

**THE EFFECTIVE DIFFUSION DISTANCE FOR THE SINTERING OF
NANOCRYSTALLINE CERAMIC POWDERS**

by

Tiandan Chen

B. E., Tongji University, China 2000

Master of Science, University of Pittsburgh, 2006

Submitted to the Graduate Faculty of
The Swanson School of Engineering in partial fulfillment
of the requirements for the degree of
Doctor of Philosophy

University of Pittsburgh

2008

UNIVERSITY OF PITTSBURGH
SWANSON SCHOOL OF ENGINEERING

This dissertation was presented

by

Tiandan Chen

It was defended on

October 16, 2008

and approved by

John A. Barnard, Professor, Department of Mechanical Engineering and Materials Science

Pradeep P. Fulay, Professor, Department of Mechanical Engineering and Materials Science

Jörg M.K. Wiezorek, Associate Professor, Department of Mechanical Engineering and

Materials Science

William S. Slaughter, Associate Professor, Department of Mechanical Engineering and

Materials Science

Dissertation Director: Ian Nettleship, Associate Professor, Department of Mechanical

Engineering and Materials Science

Copyright © by Tiandan Chen
2008

THE EFFECTIVE DIFFUSION DISTANCE FOR THE SINTERING OF NANOCRYSTALLINE CERAMIC POWDERS

Tiandan Chen, PhD

University of Pittsburgh, 2008

Traditional geometrical models of intermediate stage sintering assume that pores are present at every grain edge. In consequence, the grain size is used as a measure of microstructural scale for the prediction of densification kinetics for ceramic materials. In this study, scanning electron micrographs of ZrO_2 -3mol% Y_2O_3 and hydroxyapatite that had been pressed to a green density of 46% and isothermally sintered at 1275°C and 1100°C respectively, showed multiple grains between pores. Measurements of the pore size, grain size and pore size distribution indicated that contrary to the assumption of the traditional models of sintering, pore neck elimination was involved in densification and coarsening during intermediate stage sintering. Thus the pore separation rather than the grain size should correlate with diffusion length in this material. Similar results were also found for previously studied α - Al_2O_3 . However, the expected power law relationship between densification rate and microstructural scale does not fit the data well for pore separation. A new experimentally measured effective diffusion distance based on the arrangement of pores is proposed to predict the effect of microstructure on densification behavior. This effective diffusion distance will allow simple one dimensional flux models like the combined stage sintering model to be adapted for analyzing the sintering of spatially heterogeneous ceramic materials by both pore shrinkage and pore elimination.

TABLE OF CONTENTS

| | |
|---|------|
| TABLE OF CONTENTS | V |
| LIST OF TABLES | VIII |
| LIST OF FIGURES | IX |
| ACKNOWLEDGEMENTS | XIII |
| 1.0 INTRODUCTION..... | 1 |
| 2.0 BACKGROUND | 3 |
| 2.1 SINTERING | 3 |
| 2.1.1 Driving force of sintering | 3 |
| 2.1.2 Flux of atoms | 4 |
| 2.1.3 Sintering stages..... | 7 |
| 2.1.4 Traditional model of single-phase sintering and its capability | 10 |
| 2.2 COMBINED-STAGE SINTERING MODEL..... | 13 |
| 2.3 EFFECT OF POWDER PROCESSING VARIABLES..... | 17 |
| 2.3.1 Effects of powder processing on green density..... | 18 |
| 2.3.2 Effects on densification and microstructure evolution..... | 20 |
| 2.4 SYSTEMS UNDER STUDY | 24 |
| 2.4.1 Zirconia..... | 24 |
| 2.4.2 Hydroxyapatite ($\text{Ca}_{10}(\text{PO}_4)_6(\text{OH})_2$) | 29 |

| | | |
|-------|---|----|
| 2.4.3 | α -Alumina..... | 30 |
| 3.0 | HYPOTHESIS..... | 36 |
| 4.0 | OBJECTIVE | 37 |
| 5.0 | EXPERIMENTAL PROCURE | 38 |
| 5.1 | SAMPLE PREPARATION | 38 |
| 5.1.1 | Preparation of green bodies | 38 |
| 5.1.2 | Sintering..... | 39 |
| 5.1.3 | Sample section and preparation for polishing..... | 40 |
| 5.1.4 | Grinding and polishing..... | 40 |
| 5.1.5 | Thermal etching | 41 |
| 5.2 | MICROSCOPY..... | 41 |
| 5.3 | DATA ANALYSIS | 42 |
| 5.3.1 | Measurement of densities | 42 |
| 5.3.2 | Calculation of isothermal densification rate..... | 43 |
| 5.3.3 | Measurement of average pore separation and grain size..... | 43 |
| 5.3.4 | Analysis of solid area fraction and number of pores per unit area.... | 45 |
| 5.3.5 | Measurement of effective diffusion distance in the proposed work... | 46 |
| 6.0 | RESULTS AND DISCUSSION | 49 |
| 6.1 | DENSIFICATION | 49 |
| 6.2 | GRAIN INTERCEPT, PORE SIZE AND PORE SEPARATION..... | 52 |
| 6.3 | EFFECTIVE DIFFUSION DISTANCE OF SYSTEMS UNDER STUDY... | 68 |
| 7.0 | CONCLUSIONS | 78 |
| 8.0 | SUGGESTED FUTURE WORKS | 80 |

BIBLIOGRAPHY..... 81

LIST OF TABLES

| | |
|--|-----------|
| Table 1: Properties of 99.5% alumina. | 33 |
| Table 2: Comparisons of densities measured by Archimedes and images | 62 |
| Table 3: Flux field width of grain boundary diffusion and volume diffusion in different microstructures. | 71 |

LIST OF FIGURES

| | |
|--|----|
| Figure 1: Illustration of the two-sphere sintering model geometry. The neck radius is given by r and the particle radius is a | 4 |
| Figure 2: (a) Initial stage of sintering; model structure represented by spheres in tangential contact. (b) Near end of initial stage. Spheres have begun to coalesce. The neck growth illustrated is for center-center shrinkage of 4%. (c) Intermediate stage; dark grain have adopted shape of tetrakaidecahedron, enclosing white pore channels at grain edges. (d) Final stage; pores are tetrahedral inclusions at corners where four tetrakaidecahedra meet..... | 8 |
| Figure 3: Early phenomenological models for intermediate stage and final stage of sintering. | 10 |
| Figure 4: The: The illustration of a fundamental two-dimensional section model which is common to all microstructures during all the sintering stages..... | 13 |
| Figure 5: The: Cell construction in the left showing a grain and its associated porosity, at initial stage sintering (after DeHoff). | 16 |
| Figure 6: The Illustration of agglomerated particles..... | 18 |
| Figure 7: The illustration of pore arrangement after some pore elimination. | 21 |
| Figure 8: The illustration of non-random pore arrangement in sintered aggregated nanopowders. | 22 |
| Figure 9: The thermal hysteresis loop of the phase transition between monoclinic and tetragonal zirconia. | 24 |
| Figure 10: Fraction of ZrO_2 - Y_2O_3 phase diagram..... | 25 |
| Figure 11: Illustration the effect of particle volume expansion on surrounding cracks. | 26 |
| Figure 12: Large tensile stresses generated around a crack can stress induce the tetragonal to monoclinic phase transformation in a process zone around the crack tip. The expansion thus absorbs energy therefore extra work needed to extend crack through the area. | 27 |
| Figure 13: Cubic zirconia used as a solid electrolyte for solid oxide fuel cell. | 29 |
| Figure 14: A (0001) plane with only one layer of atoms of typical corundum structure is shown here. | 30 |

| | |
|---|-----------|
| Figure 15: Demonstration of a $\{10\bar{1}0\}$ type plane of a typical corundum structure. | 31 |
| Figure 16: Demonstration of a unit cell of $\alpha\text{-Al}_2\text{O}_3$. | 32 |
| Figure 17: The transformation sequence between Boehmite to Corundum. | 33 |
| Figure 18: Diagrammatic demonstration for the heating procedure used in this experiment. | 39 |
| Figure 19: Showing the density slice operation in which the top line in left toolbar is dragged to adjust the contrast of image when “Density Slice” command was performed. | 45 |
| Figure 20: The original SEM image (left) and the binary image converted from it by software “ScionImage” (right). | 46 |
| Figure 21: The illustration of pore boundary tessellation. | 47 |
| Figure 22: An example of distance map obtained from tessellator. | 48 |
| Figure 23: The effect of sintering time on solid volume fraction of $\text{ZrO}_2\text{-3mol\%Y}_2\text{O}_3$. | 49 |
| Figure 24: The effect of sintering time on solid volume fraction of hydroxyapatite. | 50 |
| Figure 25: The relationship for isothermal sintering of TZ-3YB between Volume Strain Rate and Solid Volume Fraction. The dash blue curve is power fitting of data points. | 51 |
| Figure 26: The relationship for isothermal sintering of HA between Volume Strain Rate and Solid Volume Fraction. The dash pink curve is power fitting of data points. | 52 |
| Figure 27: The average grain and pore intercept length plotted against solid volume fraction for TZ-3YB samples. | 53 |
| Figure 28: The average grain, pore and pore separation intercept length plotted against solid volume fraction for TZ-3YB samples. | 54 |
| Figure 29: Plot of Ratio of average pore separation intercept length and grain intercept length against Solid Volume Fraction of TZ-3YB samples. | 55 |
| Figure 30: Plot of log volume strain rate against log inverse intercept length (grain and pore separation) of TZ-3YB. | 56 |

| | | |
|-------------------|--|-----------|
| Figure 31: | The average grain, pore and pore separation intercept length plotted against solid volume fraction for HA samples..... | 57 |
| Figure 32: | Plot of log volume strain rate against log inverse intercept length (grain and pore separation) of HA. | 57 |
| Figure 33: | Comparison of Ratios of average pore separation intercept length over grain intercept length as isothermal sintering time increase among TZ-3YB, HA and dispersed alumina samples..... | 58 |
| Figure 34: | Number of pores per unit area of TZ-3YB decrease rapidly as isothermal sintering time increases. | 59 |
| Figure 35: | Plot of log volume strain rate against log inverse intercept length (grain and pore separation) of dispersed alumina samples. | 59 |
| Figure 36: | A high magnification SEM image shows there is no vacancy in triple point in the polished cross-section of these zirconia ceramics. | 60 |
| Figure 37: | A two dimensional representation of a microstructure with more than one grain between pores. Vacancy annihilation on boundary between grain 1 and grain 2 would create tension without mass transport along boundaries between grain 1 and grain 3 and boundaries between grain 2 and grain 3 in response to stress. | 63 |
| Figure 38: | The non-random pore arrangement by in TZ-3YB samples SEM observation. Pores appear to reside more at the boundaries of dense regions containing many grains as schematically..... | 64 |
| Figure 39: | The illustration of non-random pore arrangement. (a): The comparison of intercept lengths λ_{ps} and the distances λ_i needed to calculate for λ_d. (b): The demonstration of cores and shells..... | 65 |
| Figure 40: | The schematic drawing of pore arrangement and how the effective diffusion distance can be defined..... | 67 |
| Figure 41: | The plot of volume strain rate against inverse effective diffusion distance of TZ-3YB..... | 68 |
| Figure 42: | The plot of volume strain rate against inverse effective diffusion distance of HA. | 69 |
| Figure 43: | Simple one dimensional model: (a) pores separated by single grain. (b) pores are separated by multiple grains. | 72 |
| Figure 44: | Simple two dimensional model from traditional models with pores locate on every grain edges..... | 73 |
| Figure 45: | Ratio of average pore intercept length over grain intercept length of HA samples..... | 74 |

Figure 46: Plots of volume strain rate against inverse effective diffusion distance of alumina ceramics. 75

Figure 47: Comparison of Ratios of average pore separation intercept length over grain intercept length as isothermal sintering time increase between HA and alumina samples. 76

ACKNOWLEDGEMENTS

I would like to begin to thank my advisor, Professor Ian Nettleship, for his guidance and support throughout my graduate study at the University of Pittsburgh. I would also like to thank precursors of our porous materials laboratory, especially Dr. Richard John McAfee, Jr. My research in this laboratory began from the experimental skills and knowledge taught by him. The members of my thesis committee, Prof. John A. Barnard, Prof. Pradeep P. Fulay, Prof. William S. Slaughter and Jörg M. K. Wiezorek, are gratefully acknowledged for their essential technical and philosophical input of this work. The faculty, staff, and students of the Materials Science & Engineering Departments have greatly enriched my experience at the School of Engineering, making past years an enjoyable memory for me. Also, the encouragement and support of my family, especially my husband, Yang Dong, makes me more motivated in pursuing my education. Last but not least, financial support from the Sandia National Laboratory is gratefully acknowledged.

1.0 INTRODUCTION

Sintering commonly refers to processes of consolidating a body shaped from powder particles which involves heat treatment at elevated temperatures, usually at $T > 0.5T_m$ [K] (T_m is the melting temperature for that specific material). Diffusional mass transport is appreciable in this elevated temperature range. Usually a self-supporting compact is obtained by pressing, casting or other processing before sintering. Almost all aspects of the sintering process have been addressed in many books and publications.^{1,2,3,4,5}

Polycrystalline ceramic material is one very common category which would receive sintering treating. Ceramic processing is based on the sintering of powder compacts rather than melting, forging or other methods. The reasons for that are addressed below. First, ceramics usually melt at high temperatures, which makes melting difficult and inefficient. Second, ceramics are brittle which is not suitable for processing by thermo-mechanical forming. While sintering of ceramic materials has been practiced since the beginning of human civilization the process is still not understood to the point that the effects on shrinkage and microstructure can be accurately predicted.

In response to the inability of the early phenomenological models to predict sintering shrinkage and shape change under most practical circumstances, attention was paid to continuum modeling. The continuum models that have been developed for the prediction of shrinkage have been comprehensively reviewed by Olevsky.⁶ Examples include viscoplastic approaches, such as

that of Besson and Abouaf ⁷ and the more common viscous models, such as that of Scherer and Bordia. ⁸ Often, the only microstructural variable in these models is density or more precisely, the solid volume fraction. However, the phenomenological contact flattening models ^{9,10} can be used for time and temperature compensation in the continuum model. Unfortunately, the large number of material constants and variables required leads to a situation wherein material data such as activation energies become adjustable parameters in a curve fitting exercise. ¹¹ To a certain extent, this can be mitigated by calibration of material properties, such as uniaxial viscosity, in thermal treatments that faithfully reproduce aspects of the sintering cycle. ^{12,13} While the continuum approach has provided a very practical method for predicting sintering shrinkage, it is not capable of direct representation of internal variables, such as particle packing arrangement, particle rearrangement, and grain growth, that are known to affect the final density and the microstructural evolution. In response to this problem, there is now another shift about to take place in the modeling to three-dimensional mesoscale microstructural simulation of sintering. ¹⁴

The study addressed in this thesis started from the basic single phase sintering using aggregated nanocrystalline zirconia and hydroxyapatite powders and a less aggregated sub micron alumina powder. The goal is to provide a parameter that may allow a simple one dimensional flux model to be used to analyze densification of spatially inhomogeneous structures and to provide a better understanding of how powder processing effect the sintering for aggregated nanocrystallize powders. This information will be required to introduce the effects of microstructure into the predictions of the general kinetic models such as the master sintering curve.

2.0 BACKGROUND

2.1 SINTERING

2.1.1 Driving force of sintering

The driving force for densification and coarsening during sintering is the decrease in the surface free energy of powder compacts. Since Γ_{sv} (surface free energy of the solid-vapor interface) is normally greater than Γ_{ss} (surface free energy of the solid-solid interface), the solid-vapor interfaces tend to be replaced by solid-solid interface when enough energy is provided. This driving force is illustrated by Fig. 1. The two spheres model is commonly used for the initial stage of sintering. The intermediate stage and final stage of sintering use different geometrical models while the driving forces and diffusion mechanisms are the same.

The starting point for predicting shrinkage is usually the Gibbs-Thompson-Freundlich equation shown below, which describes the equilibrium concentration of vacancies under a curved surface (c) based on vacancy concentration for a flat surface (infinite curvature, c_0),¹⁵

$$c = c_0 \exp \left[\frac{\gamma V_m}{RT} \left(\frac{1}{r_1} + \frac{1}{r_2} \right) \right] \quad \text{Equation (2.1)}$$

Where r_1 and r_2 are the principle radii of curvature for the curved surface, V_m is the molar volume, γ is the energy per unit area of the surface, R is the gas constant, and T is the absolute temperature. The radii of curvature for a convex surface, such as the particle surface, are positive. However, in the concave neck region the radius in the plane of the contact area between the particles will be positive but the radius in the plane of the particle centers will be negative. In Fig.1 which illustrates neck growth between two particles, the radius of particles, a , is positive and the radius of the neck, r , is negative, which results in a greater vacancy concentrations under the surface of the neck. Thus mass is driven to transport toward the surface of the neck from the convex surface or from the grain boundary.

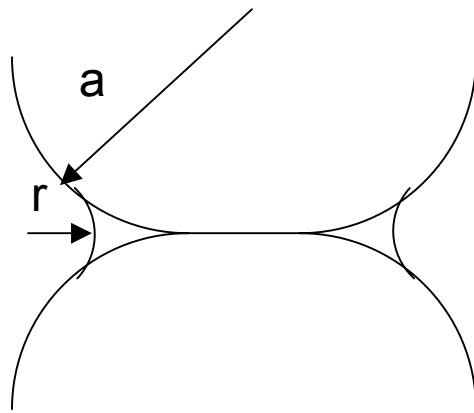


Figure 1: Illustration of the two-sphere sintering model geometry. The neck radius is given by r and the particle radius is a .

2.1.2 Flux of atoms

Diffusion is among the most important phenomena observed in sintering of ceramic materials. The diffusion of atoms is generally necessary for changes in microstructure to take place in processes such as the densification of powder compacts, creep deformation at high temperatures, grain growth, and the formation of solid-state reaction products and in solid ionic

conductors. Atomic diffusion rate is largely dependent on the type of defects present and their concentrations.

Diffusive mass transport takes place when there is a gradient in the chemical potential and when the species in question has sufficient mobility. In continuum diffusion, transport is described by solutions to Fick's first and second laws, under geometric and concentration boundary conditions, which are determined by the experimental configuration. Fick's first law (in one dimension):

$$J = -D \left(\frac{dC}{dx} \right) \quad \text{Equation (2.2)}$$

states that the atom flux J (number per unit area per unit time) at a steady state is proportional to the concentration gradient dC/dx . The proportionality constant D is termed the diffusion coefficient or diffusivity, and is usually written in units of cm^2/sec .

Fick's second law describes the accumulation or depletion of concentration, C , when steady-state conditions are not achieved, and is obtained from the spatial derivative of the flux:

$$\frac{\partial C}{\partial t} = -\frac{\partial J}{\partial x} = D \left(\frac{\partial^2 C}{\partial x^2} \right) \quad \text{Equation (2.3)}$$

The diffusional flux of atoms at the neck, j_a , during sintering of a pure compound is governed by Herring's equation, the general flux equation, which is shown below,

$$j_a = -\frac{D}{\Omega_a K_B T} \nabla(\mu_a - \mu_v) \quad \text{Equation (2.4)}$$

where μ_a and μ_v are the chemical potentials of the atoms and vacancies, respectively, $\nabla(\mu_a - \mu_v)$ is the chemical potential gradient related to curvature which drives mass transport, $D/k_B T$ represents the mobility term for either grain-boundary or volume diffusion, k_B is Boltzmann's constant, D is the diffusivity, T is absolute temperature, and Ω_a is the atomic volume.

There are a number of competing paths for mass transport during ceramic sintering, such as grain boundary diffusion, volume diffusion and surface diffusion. Some of these, usually surface diffusion, leads to coarsening, which is the growth of the neck between particles leading to reduction of the specific surface area without approach of the particle centers. Other transport mechanisms, normally volume diffusion and grain boundary diffusion lead to densification, which is defined as neck growth with approach of particle centers. In densification mechanisms (in the absence of viscous flow and plastic deformation), the grain boundary plane serves as the “source” for diffusional transport, and the neck as the “sink” or repository for atoms.

Identifying the diffusing species can be quite complicated for ionic solids. Consider Zirconia containing 3 mol% yttria which is one of the materials used in this study. The common defect equation for this ceramic material is listed below:



The diffusion species seems to be O^{2-} according to the defect equation. However, since in both tetragonal zirconia and cubic stabilized zirconia, $D_O^l \gg D_{Zr}^l$, oxygen will not control the rate of sintering. In fact a complex diffusion coefficient D_{comp} must be defined which can better describe this oxide. $D_{comp} = D_{Zr}^l + (\pi/d)\delta D_{Zr}^b$, where D_O^l and D_{Zr}^l are the oxygen and zirconium lattice diffusion coefficients, respectively, D_{comp} is the complex diffusion coefficient, D_{Zr}^b is the zirconium boundary diffusion coefficient, d is the grain size and δ is the boundary width. Okamoto *et al* calculated the D_{comp} for this yttria doped zirconia material¹⁶ from creep data and the equation¹⁷ listed below.

$$\dot{\epsilon} = \frac{14\sigma\Omega D_{comp}}{d^2 kT} \quad \text{Equation (2.6)}$$

where $\dot{\epsilon}$ is the strain rate, σ is the stress, Ω is the molecular volume, d is the grain size, T is the absolute temperature, and k is the Boltzmann's constant. Their results were comparable with the interdiffusion coefficient for Zr-Hf in cubic zirconia,¹⁸ suggesting that $D_{comp} \approx D_{Zr}^l$. Thus, it has been argued that in this Y_2O_3 stabilized cubic zirconia material, the mass transportation is controlled by the cation lattice diffusion. In summary, the rate controlling diffusion species for zirconia is thought to be Zr^{2+} , not O^{2-} . In comparison, there is little information concerning the diffusing species in hydroxyapatite while the sintering of alumina is generally believed to be controlled by the diffusion of oxygen, this being the largest ion in the structure with the slowest diffusivity.

2.1.3 Sintering stages

Classically, the process of sintering is arbitrarily divided into three stages, the initial, intermediate, and final stages based on physical reasoning so as to arrive simple geometries for densification by contact flattening. Fig. 2 demonstrated the model geometry of the three stages of sintering, which have been chosen to simplify the problem of developing solutions for densification based on the flux equations.

(a) The initial stage of sintering

At the initial stage of sintering powder particles are assumed to deform and the contact points between particles flatten to form necks without significant densification. The surface of necks forms saddles with negative curvature. Usually, initial stage sintering is considered to be complete after at most 10% densification. This typically occurs in the early stages of heating in

most practical applications of sintering. For example, the green densities of the zirconia samples used in this study were 0.45. Therefore, using the above criteria, the end of initial stage of

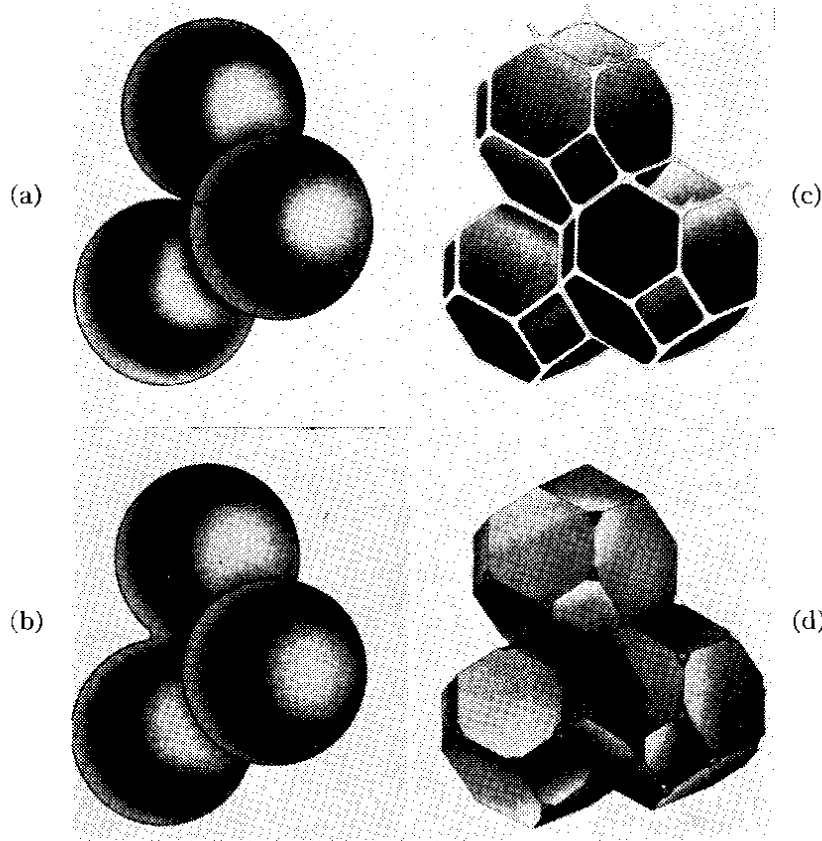


Figure 2: (a) Initial stage of sintering; model structure represented by spheres in tangential contact. (b) Near end of initial stage. Spheres have begun to coalesce. The neck growth illustrated is for center-center shrinkage of 4%. (c) Intermediate stage; dark grain have adopted shape of tetrakaidecahedron, enclosing white pore channels at grain edges. (d) Final stage; pores are tetrahedral inclusions at corners where four tetrakaidecahedra meet.¹⁰

sintering would have been reached when the solid volume fraction of those samples reached a value of 0.55 during heating, which were achieved well before the isothermal sintering stage. Since the solid-vapor interface area is large at the beginning of sintering, the driving force for sintering is also large, and initial stage of sintering will be completed in seconds or minutes when subjecting samples to a high temperature environment. The zirconia materials used in this study achieved at least 25% densification after heating and being held at the target temperature for 6

minutes. It can therefore be concluded that isothermal experiments in most circumstances will not examine initial stage sintering.

(b) Intermediate stage of sintering

During the intermediate stage of sintering, neck growth occurs and interconnected porous channels are formed. The microstructure evolves into a complex structure of interpenetrating networks of grains and pores. The compact shrinks and densifies up to a value above 0.9 in solid volume fraction. The particle contacts continue to flatten allowing the particles centers to approach. Besides densification and shrinkage other phenomena can occur. For example, coarsening would happen if the material transport originates on the surface of particles. Coarsening and grain growth reduces the surface energy of the system and decreases the driving force for densification. Thus, in isothermal sintering, the densification rate decreases as the neck sizes increase. In most case, grain growth and grain coarsening are not desirable since these processes lead to large grain sizes, while high density and fine grains of ceramics are the goals of most studies. For systems that densify well there tends to be little grain growth in intermediate sintering due to pinning of grain boundaries by a uniform distribution of fine pore channels.

(c) Final stage of sintering

After sintering reaches the final stage, pores become isolated and the solid volume fraction of materials exceeds about 0.92. Ideally, at the end of the final stage of sintering, all pores are eliminated and materials are 100% dense. However, there are commonly randomly distributed residual pores present in the material.

It must be stated at this point that these description of the stages of sintering are qualitative broad and fail to capture the real complexity of microstructure evolution. Their main

purpose has been to highlight the main issues and provide the foundation for phenomenological modeling.

2.1.4 Traditional model of single-phase sintering and its capability

Simple geometries have been used to model the microstructure evolution during the stages of sintering. As shown in Fig. 3, in early phenomenological models the microstructure of

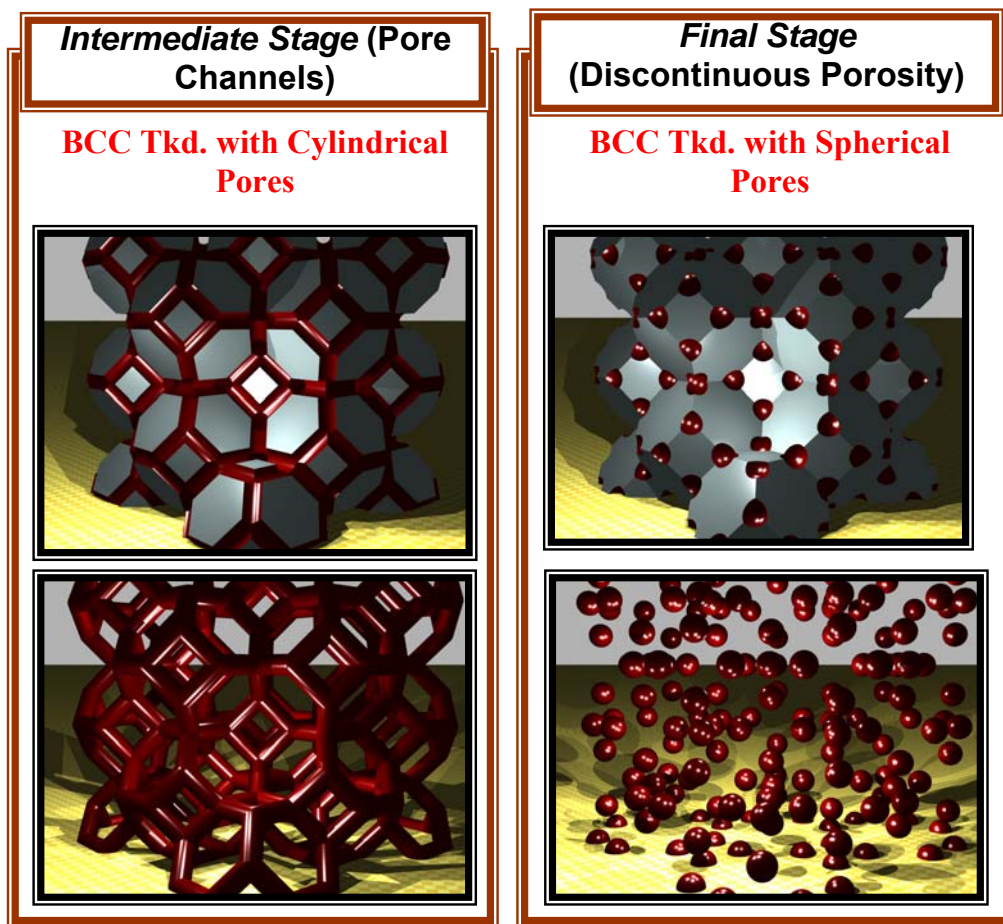


Figure 3: Early phenomenological models for intermediate stage and final stage of sintering. Pictures in above are packing of spheres. Pictures in below are porous structures.¹⁹

initial stage models were commonly represented by ordered arrays of spheres. In contrast, intermediate stage and final stage of sintering are based on space filling tetrakaidecahedrons. The

difference between the latter two stages is the pores are interconnected cylindrical channel located on the 36 edges of the tetrakaidecahedrons for intermediate stage. While in the model for the final stage of sintering, pores are spheres located on all 24 corners.

In these early models, the geometries allow uniform shrinkage as densification proceeds and the distance between particle centers decreases as the flat contacts between the particles grow. The ways in which adjacent contacts impinge upon each other determine the ranges of solid volume fraction over which these models can be applied. For example, if spheres are packed in a simple cubic arrangement, the solid volume fraction ranges from approximately 0.52 (point contact between particles) to 0.82 (contact between necks, which would form a new grain edge and break the geometrical constraints of the model). If spheres are face centered cubic packed, the solid volume fraction may range from 0.72 (by pore to pore contact) to full density. Obviously, perfect packing cannot be achieved in real materials due to non-uniform packing and irregular shaped particles.

Other initial stage geometries such as dense random packing²⁰ can also be found in the literature. But common to all these traditional sintering models is the requirement that the problem of representing sintering microstructures can be reduced to a representative volume containing a single particle and its attendant porosity. That is to say, the diffusion length is determined by the particle size or grain size and that the grain size can scale the shrinkage of a ceramic on sintering to the diffusion length.²¹ However, if compacts were formed by non-equisized particles or irregular packing, the real microstructures cannot be well represented. Thus a means of imposing a distribution of particle or pore size cannot be provided by these models because of the geometric constraints. The models rely on the effects of these issues on grain size

and therefore scale. Similarly the models cannot implicitly address different particle packing arrangements and the consequent effect of green density.

The models are also not directly capable of representing grain growth or coarsening. If the geometrical constraints are to be represented, only a self-similar scaling of the microstructure can occur. Nettleship *et al* reported that non-dimensional parameters can be used to make direct comparisons of coarsening between densification models and experiments, independent of scale.²² As defined in equations (2.7) and (2.8), the two non-dimensional parameters used are the surface area ratio (ψ), which is the ratio of the surface areas of solid/solid to solid/vapor boundaries, and the intercept ratio (Λ), which is the ratio of mean grain to pore intercept lengths.

$$\psi = \frac{S_V^{SS}}{S_V^{SV}} \quad \text{Equation (2.7)}$$

$$\Lambda = \frac{\lambda_g}{\lambda_p} \quad \text{Equation (2.8)}$$

The predicted evolutions of these parameters during densification in the simple geometric models have been previously determined.²³ Because ψ and Λ are independent of the length scale of the microstructure, they are unaffected by self-similar coarsening from the fixed microstructural geometry assumed in the models. ψ is better than Λ for final stage sintering evaluation because of the assumption that all pores are on grain boundaries in the definition of λ_g . The final stage sintering model commonly underestimates ψ , which can be explained by the fact that pores in the model are too small relative to the grains and therefore some grain edges and grain corners do not contain pores in the real materials.

Unlike the phenomenological models, which only allow densification, Weiser and De Jonghe observed regions of de-densification in real microstructures in which some necks are broken to facilitate the rearrangement of particles.²⁴ The processes of particle rearrangement are

not addressed in the commonly used phenomenological models. It was concluded that the non-uniform arrangement at particles in real sintering microstructures result in particle rearrangement by differential densification, local densification or de-densification. However the simple phenomenological models continue to be applied to predict the effect of porosity on densification kinetics. ²⁵ While there is some success in predicting densification kinetics, the limited representation of microstructure evolution and the severe effect of microstructure on densification rate may inhibit the widespread use of these models in manufacturing.

2.2 COMBINED-STAGE SINTERING MODEL

One important example of traditional models is the combined stage model. Hansen *et al* derived a single equation that quantifies sintering as a continuous process from the beginning to end by focusing on the similarities between the three stages of sintering. ²⁶ Details have been provided by Hansen *et al* in the same paper. They proposed a fundamental two-dimensional section model as shown in Fig. 4, which is common to all microstructures during all the sintering

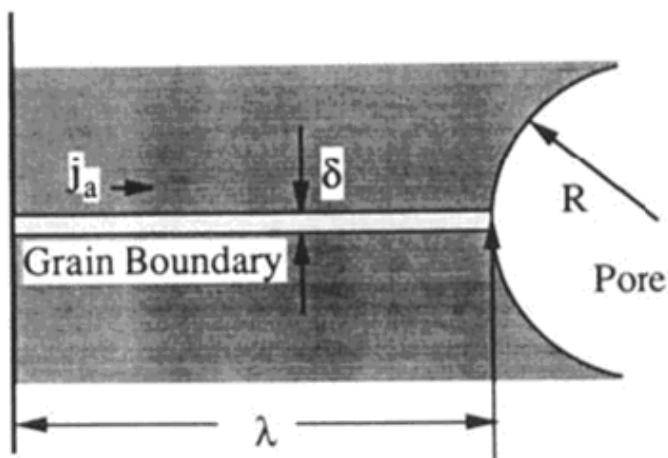


Figure 4: The: The illustration of a fundamental two-dimensional section model which is common to all microstructures during all the sintering stages. ²⁷

stages. In general, the edge of the diffusion field is on the center of the necks between two sintering particles during the initial stage or on half of the distance between nearest-neighbor pores for the other stages.

The diffusional flux of atoms is governed by the Herring's equation in equation (2.4),²⁸

$$j_a = -\frac{D}{\Omega_a k_B T} \nabla(\mu_a - \mu_v) \quad \text{Equation (2.4)}$$

The chemical potential gradient at the pore surface will be controlled by two terms, the curvature, K , which is proportional to it, and the distance over which material is drawn to the pore, λ , which is inversely proportional to it. The scaling parameters which relate these terms to the particle or grain diameter, G , are assumed by the following relationships:

$$K = -\frac{C_k}{G} \quad \text{Equation (2.9)}$$

$$\lambda = C_\lambda G \quad \text{Equation (2.10)}$$

where the curvature of pore is taken as negative. Thus, the chemical potential gradient at the surface of the pore is

$$\nabla \mu_{a|s} = -\frac{\alpha \gamma \Omega_a C_k}{C_\lambda G^2} \quad \text{Equation (2.11)}$$

where α depends solely on the three-dimensional geometric relationship between sources and sinks of material along the grain boundary, which is a constant of proportionality relating the gradient to λ , and γ is the surface energy.

Combining equations (2.4) and (2.11), the equation representing the normalized flux of atoms arriving at the surface of the generalized pore shown in Fig. 4 by either volume or grain-boundary diffusion is listed below:

$$j_{a|s} = \frac{D}{K_B T} \left(\frac{\alpha \gamma C_k}{C_\lambda G^2} \right) \quad \text{Equation (2.12)}$$

If the diffusion distances and curvatures for the body can be expressed in terms of meaningful averages, this summation, which multiplies the average local flux for grain-boundary and volume diffusion by the area available for diffusion, is given by

$$J = \frac{1}{2} j_{asb} \delta L_b + j_{asv} A_v \quad \text{Equation (2.13)}$$

In general, L_b and A_v are unknown, but for any microstructure they are assumed to scale with G and G^2 respectively. The scaling factors for the areas available for diffusion are defined in equations (2.14) and (2.15).

$$\frac{1}{2} L_b = C_b G \quad \text{Equation (2.14)}$$

$$A_v = C_v G^2 \quad \text{Equation (2.15)}$$

Where C_b and C_v are constants.

When applied to the DeHoff cell model, (shown in Fig. 5) atomic flux will result in shrinkage of the centroid-base distance by dh_p and expansion of the grain-boundary area of the pyramid S_p^b (see Fig. 5). Although S^b and h are not known for a general microstructure, they are also again assumed to scale with grain size as

$$S^b = C_a G^2 \quad \text{Equation (2.16)}$$

$$h = C_h G \quad \text{Equation (2.17)}$$

They use the dimensionless geometric parameter Γ to comprise five scaling factors that relate specific microstructural feature to the scale (grain diameter). Two parameters shown below

lump the assumed dependencies of driving force and flux to the scale of the microstructure (grain size).

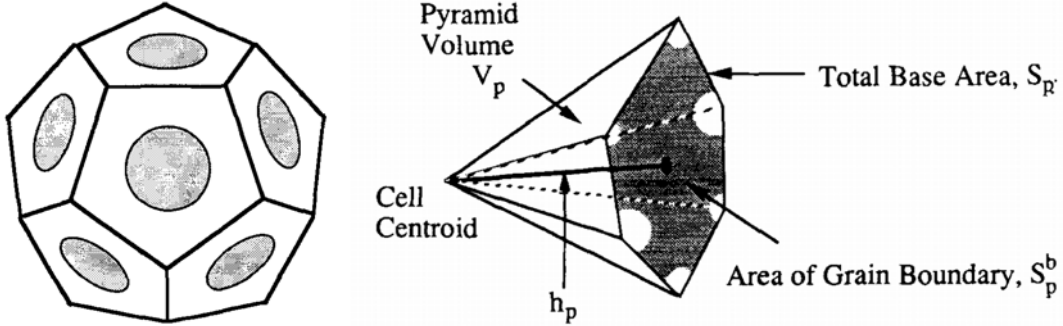


Figure 5: The: Cell construction in the left showing a grain and its associated porosity, at initial stage sintering (after DeHoff²⁹). The shaded areas represent solid contact areas between cells, i.e., grain boundaries. Pyramid subgeometry of a cell is shown in the right side.

$$\Gamma_b = \frac{aC_k C_b}{C_\lambda C_a C_h} \quad \text{Equation (2.18)}$$

$$\Gamma_v = \frac{aC_k C_v}{C_\lambda C_a C_h} \quad \text{Equation (2.19)}$$

Thus, the overall isotropic linear shrinkage of a material that can be represented by the DeHoff cell model is

$$-\frac{dL}{Ldt} = \frac{\gamma\Omega}{k_B T} \left(\frac{\Gamma_v D_v}{G^3} + \frac{\Gamma_b \delta D_b}{G^4} \right) \quad \text{Equation (2.20)}$$

Therefore equation (2.20) relates the instantaneous linear shrinkage rate to the diffusion coefficient and other material parameters and mean grain diameter. Where γ is the surface energy, k_B is Boltzmann's constant, D is the diffusivity, T is absolute temperature, and Ω_a is the atomic volume, G is the mean grain diameter.

Since grain boundary diffusion and volume diffusion dominate at different temperature range during sintering, either D_v or D_b has a very small value when the other mechanism

dominates so that only one of the two terms in right of equation (2.20) is significant for a certain diffusion mechanism. Thus, in those traditional models, the expected relationship for grain

boundary diffusion is $\frac{\dot{\rho}}{\rho} \propto \frac{1}{G^4}$ and for bulk diffusion is $\frac{\dot{\rho}}{\rho} \propto \frac{1}{G^3}$. This implies a very strong dependence or even a dominant effect of densification rate on microstructure.

2.3 EFFECT OF POWDER PROCESSING VARIABLES

To study the densification behavior for aggregated microstructure, it will be important to understand how the green microstructure affects the microstructural evolution. A distinction will be made between the densification and microstructure evolution of micron size powders that tend to be composed of one or two crystals in a powder particle and nanocrystalline powders that tend to be aggregated.

It is now well known that there are intrinsic effects of sizes on the properties of nanoparticles that go beyond those predictions made by scaling down macroscopic properties. These effects are usually explained by the confining effect of finite size on the atomic potentials of atoms. For example, there have been reports focusing on the dependence of melting points on the size of small crystallites. For example, Buffat et al. have studied size effect on the melting temperature of gold particles³⁰ and Coombes has studied the melting of small crystallites of lead, indium and bismuth.³¹ They all observed a depression in melting point inversely proportional to the particle diameter. However, this size effect only becomes clearly visible when particle diameter is smaller than 10 nm. The average diameter of the zirconia crystals used in this study is 28 nanometers, which suggests that those samples are not expected to have such

significant deviations from bulk behaviors. Similarly, the crystallites in the HA powder were above 10nm in size and there are no reports of intrinsic nanoparticle size effects for HA powders.

2.3.1 Effects of powder processing on green density

The green densities of most ceramic compacts are well below that expected for dense packing of equal-sized spheres. The particles tend to agglomerate or clump, as illustrated in Fig. 6, smaller voids exist inside agglomerates and larger porous space existed between the agglomerates. This agglomeration is due to the Van der Waals force of attraction and condensed

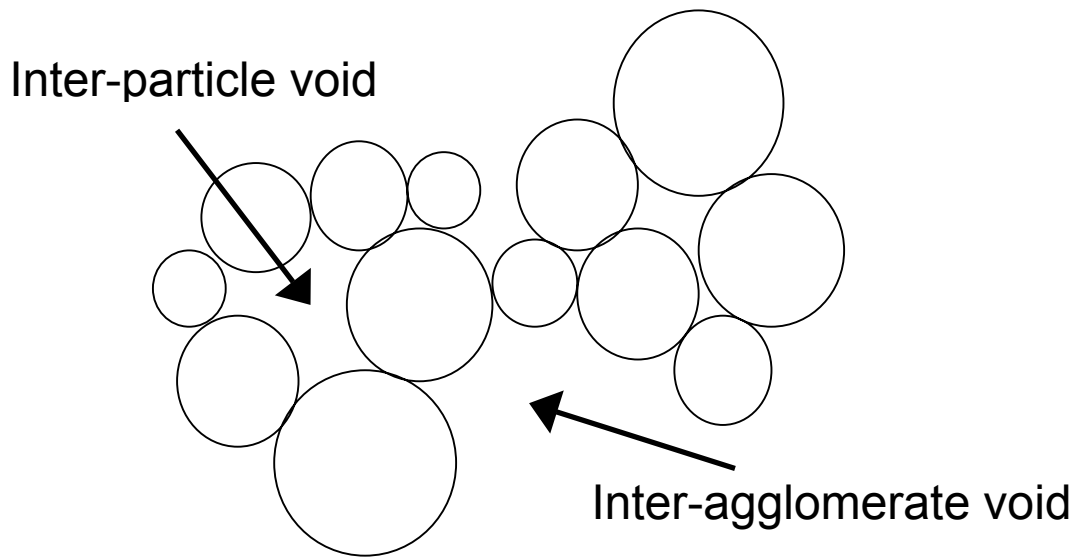


Figure 6: The Illustration of agglomerated particles.

moisture at particle contacts which tend to be stronger than gravitational forces that pull the particles apart. Therefore certain processing steps such as powder pressing, where pressure is applied, will cause the particle agglomerates to rearrange and reduce the inter-agglomerate pore volume. Inter-agglomerate voids shrink easily under pressure compared with void inside of agglomerates. This leads to a well-documented effect of pressing pressure on green density.³²

Colloidal processing can avoid the formation of the large agglomerates that necessarily occurs in powder pressing. However, for colloidal processing the agglomeration is very sensitive to the dispersion condition in the slip. Flocculation usually causes the formation of particle agglomerates that lower the green density of the ceramic.³³

i) Micron size powders

The packing behaviors of micron size powders can be different when produced by different forming methods. Both changing the dispersion condition during slip casting and pressing pressure for granulates powders can vary the green density of compacts. Zheng *et al* made a distinction between these two methods.³⁴ They suggested that pressed granulated powders have a bimodal pore population with the larger mode being the intergranular pores, which diminish as the pressure increases, while in samples fabricated by slip casting the pores are distributed unimodally in a wider range due to the lowering green density caused by flocculation.

ii) Aggregated nanocrystallize powders

The inter-particle force holding agglomerates together are much weaker than the intra-aggregate forces which bind the nanocrystals together in porous particles. The latter forces are commonly chemical bonds formed during the chemical synthesis and calcinations stages of powder preparation. Thus the green density of compacts made from aggregated nanocrystalline powders can be very low (<50%) due to heterogeneous packing. As the pressure applied on green body increases inter-agglomerate spaces shrink or are gradually filled. Thus, if various

pressures are used, the green density of compacts formed by aggregated nanocrystalline powders ranges over a greater span compared to compacts formed by micron sized powders.³⁵

2.3.2 Effects on densification and microstructure evolution

The size of particles and the particle packing can affect densification and microstructure evolution dramatically. In the traditional kinetic models, the effect of powder processing is not modeled directly but reflected through the effect of density on grain size. Separate discussions of micron size powder and nano-size powder will be used here.

i) Micron size powders

Since aggregated powder particles are less significant for micron sized powders, the whole green body densifies in a relatively synchronized fashion leading to narrow pore size distribution and pores that are small relative to the grain size which delays grain growth in final stage sintering. That is to say, shrinkage and elimination of pores occur in all area of compacts during the final stage of sintering. However, differences in packing behavior have been shown to affect both densification behavior and the onset of grain growth in intermediate stage sintering. For pressed pieces the small inter-agglomerate pores have been shown to control densification rate and shrinkage while the relatively inactive large inter-granule flaws affect only final solid volume fraction.³⁶ Also the changes in pressing pressure can affect green density, the densification behavior and the grain growth.³² For slip casting the slip dispersion has been found to affect green density, densification behavior and grain growth. Full dispersion gives the best densification and the lowest grain growth.³³ Cameron *et al* found that flocculation of an alumina powder during casting can increase grain growth at high temperatures (>1500°C), since the

diffusion length is commonly thought to be controlled by the grain size, and so a strong effect on densification is expected. There are other literature reports that grain growth associated with the sintering of heterogeneous green microstructures made by slip casting with flocculated slips may be reduced at a relatively low sintering temperature (1340°C)³⁷. However, this idea would lead to the problem that the densification behavior during sintering cannot always be explained by grain growth. Alternative explanations have been developed based on microstructural heterogeneity, although the kinetic equations were not adapted to accommodate this.

ii) Aggregated nanocrystallize powders

F. F. Lange suggested that the elimination of pores in ceramics made from aggregated powders is controlled by the coordination number of pores. Pores can only be eliminated when the coordination numbers are less than a critical value.³⁸ Thus, small pores inside of aggregated nanocrystallize powder particles are easily eliminated during the initial stage or early intermediate stage densification. On the other hand, spaces between agglomerates are not eliminated at the same rate. Thus, as sintering progresses, structures illustrated in Fig. 7 will

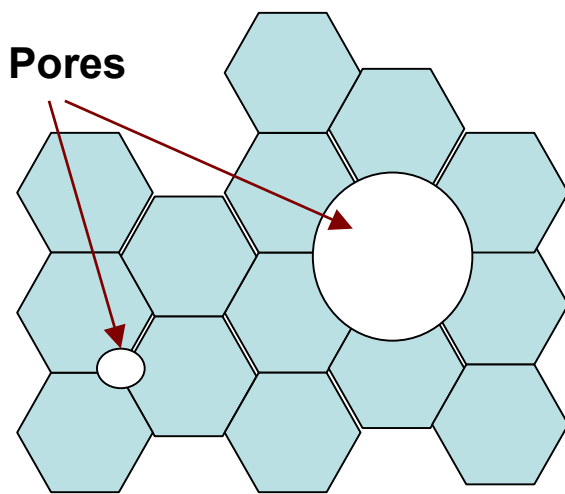


Figure 7: The illustration of pore arrangement after some pore elimination.

form. Some small pores may then be eliminated well before the structure reaches final stage sintering, and the distance between two existing pores may span across several grains. Consequently elimination of fine pores that may originate in the powder aggregates will lead to the formation of dense multigrain regions in intermediate stage sintering as illustrated in figure 8.

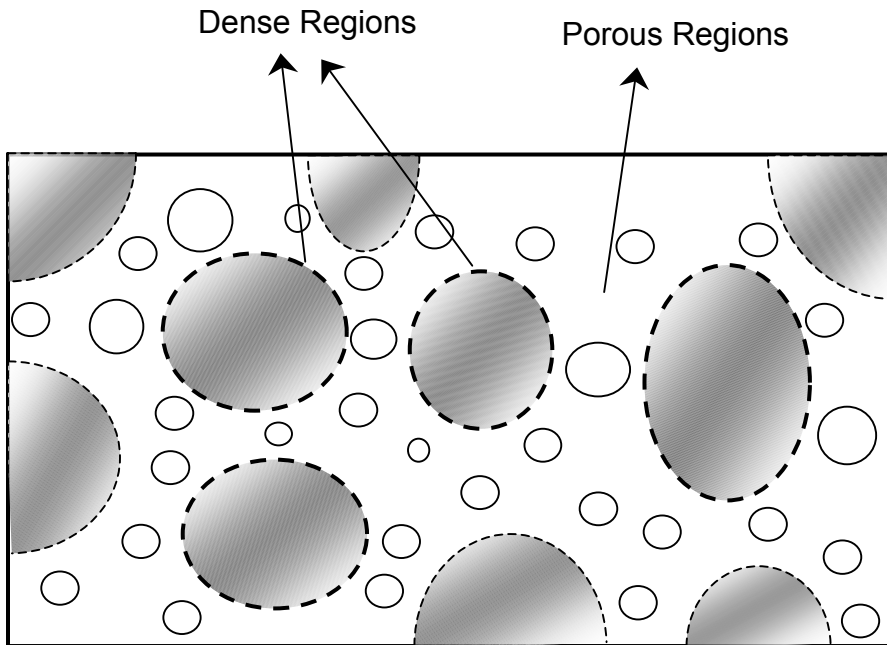


Figure 8: The illustration of non-random pore arrangement in sintered aggregated nano-powders.

This will change the number of potential mass transportation paths. The details of pore elimination in these aggregated nanocrystalline powders has not been fully investigated. Furthermore, those conceptual models, such as that of F. F. Lange³⁸, did not extend to kinetic prediction. Many studies have proposed a very strong correlation exists between grain growth and densification for nano-crystalline ceramic powders because this provides the common explanation of why nanocrystalline powders cannot be sintered at low enough temperatures to retain nanosized microstructures. Much of the emphasis has been placed on final stage sintering when grain growth becomes quite rapid in these systems. For example, Li *et al* examined the properties of ceramic pressed by a nano-crystalline alumina powders with a mean particle size of

about 10 nanometers.³⁹ They found that the average grain size of the nanoceramics increases slowly when the relative density is below 90%. In contrast, the grain grow rapidly as sintering time increase after the relative densities of the sintered Al₂O₃ nano-ceramics reached above 90%. They assume that the diffusion length for densification is controlled by grain size. Unfortunately, this has not been tested by plotting the densification rate against the inverse of grain size to evaluate the exponent.

Significantly, a two step sintering method has also been used to produce some nanoceramics with both relatively high density (above 90%) and small grain size.^{39,40} It seems that the relationship from traditional models between grain size and density does not hold in these cases because the densification rate is changing in the second step (conducted at lower temperature) but the grain size is not. The details of microstructural evolution in two step sintering have not been investigated. So it is difficult to speculate how the diffusion distance is changing in the second step, except that Wang *et al* suggested their results implied a gradual increase of pore spacing during the second step sintering.⁴¹ The fact that under this two-step sintering method high density nano-ceramics can be achieved at low temperature with no grain growth may imply the grain growth in intermediate and final stage sintering could be strongly related to the temperature but not density in these systems. Instead, the inter-pore spacing could be affected by pore elimination which would affect densification rate. Therefore, inter-pore spacing should be measured directly in these systems, because this would be sensitive to processes such as the fine pores shrinking along their length. This could potentially unify the observations made in sintering of micron sized powders and nano-crystalline powders. Some of our previous research confirms that pore elimination occurs throughout intermediate stage of sintering.⁴² Under this circumstance the diffusion distance is not correlated with grain size in the

way assumed by the models. This argument will be confirmed in this thesis and is one important motivation to design a new measure of effective diffusion distance for the sintering of aggregated nanocrystalline powders.

2.4 SYSTEMS UNDER STUDY

2.4.1 Zirconia

TZ-3YB ($\text{ZrO}_2\text{-3mol\%Y}_2\text{O}_3$ powder with binder from Tosoh Corporation, Japan) was one of systems studied in this work.

2.4.1.1 Phase transformation of zirconia

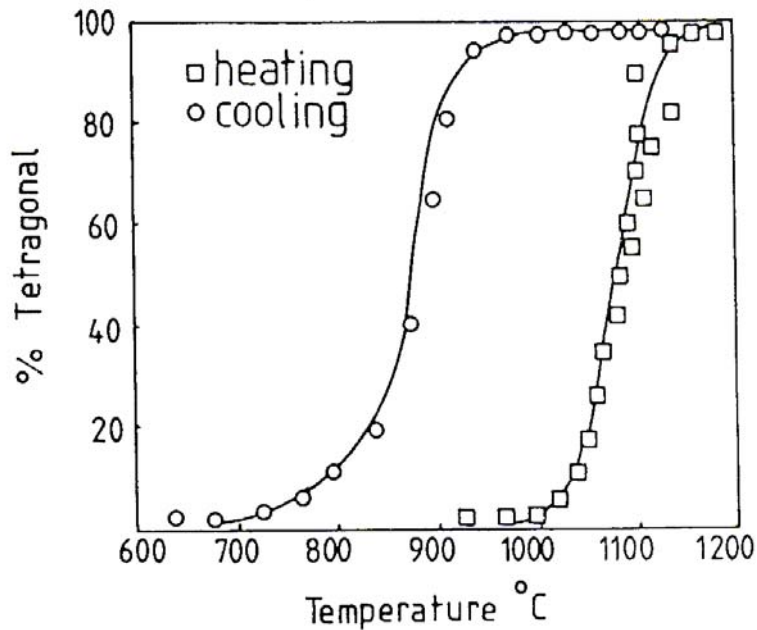


Figure 9: The thermal hysteresis loop of the phase transition between monoclinic and tetragonal zirconia. ⁴³

Zirconia exhibits three phases, monoclinic, tetragonal and cubic. Under one atmosphere of air, the transformation from tetragonal to cubic phase occurs at the temperature of 2370 °C. The transformation between monoclinic and tetragonal phases is a diffusionless shear process with a thermal hysteresis loop, as shown in Fig. 9. The grain/crystal size of zirconia will affect the transformation temperatures. Finer ZrO_2 crystals will shift the thermal hysteresis loop to lower temperatures compared to coarser crystals.

Among those three structures, tetragonal and cubic zirconia are of great interest in the

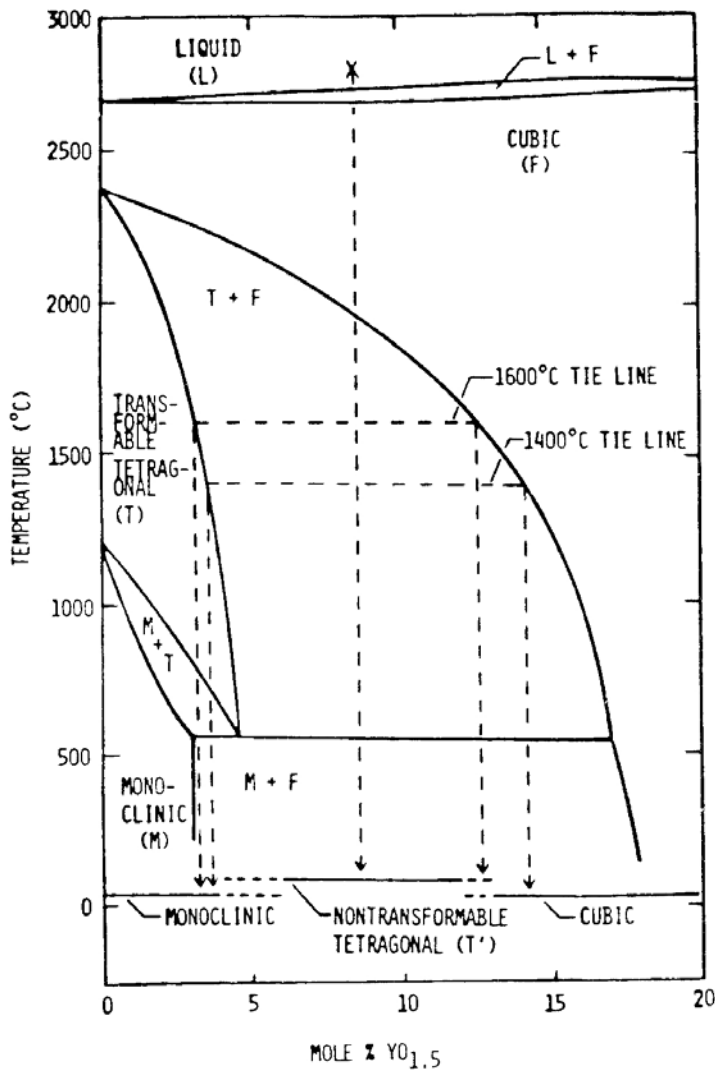


Figure 10: Fraction of ZrO_2 - Y_2O_3 phase diagram.

engineering field. Consequently, oxides, such as MgO, CaO and Y₂O₃ that dissolve in zirconia and tend to stabilize the tetragonal or cubic phase, because of their unique atom sizes, drew great attention for decades. For example, addition of Y₂O₃ can decrease the temperature of the tetragonal-monoclinic transformation, as shown in the binary phase diagram of Fig. 10. Sintering of zirconia with 3 mol % Y₂O₃ at a temperature of below 1300 °C commonly results in tetragonal sintering throughout the sintering cycle and after cooling. In this study zirconia with 3 mol % Y₂O₃ the focus was on the microstructure evolution of tetragonal zirconia.

2.4.1.2 Properties and Applications of Zirconia

Transformation of zirconia from tetragonal to monoclinic can cause an unusual 4 vol % expansion. If zirconia is incorporated into a ceramic matrix, the combination of the volume expansion and the diffusionless transformation process can lead to a phenomenon called transformation toughening. This phenomenon for zirconia-containing ceramics has been explained via two different mechanisms.

The first mechanism is microcracking. When zirconia particles are incorporated in a ceramic matrix and cooled through the tetragonal to monoclinic transformation, the volume expansion occurring in the zirconia particles causes the formation of cracks, as shown in Fig. 11.

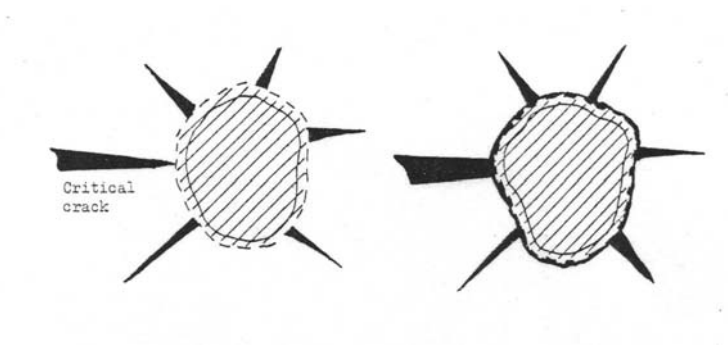


Figure 11: Illustration the effect of particle volume expansion on surrounding cracks.

The propagation of the microcracks can absorb or dissipate the energy of the main crack. Therefore the toughness of ceramic can be increased. The optimum condition for toughening to occur is when zirconia particles are large enough to transform but also small enough to cause limited microcracks.

The other and more important mechanism is called stress induced transformation toughening. To be eligible for this process, zirconia particles must be in the metastable tetragonal form at room temperature. In such a system, the large tensile stresses generated around a crack can stress induce the tetragonal to monoclinic phase transformation in a process zone around the crack tip as illustrated in Fig. 12. Then, the volume expands in the process zone and its confinement by the surrounding material result in a reduced tensile stress in the process zone. Therefore extra work and higher stress is required to move the crack through the process zone. Therefore, the toughness and the strength of the ceramic are increased.

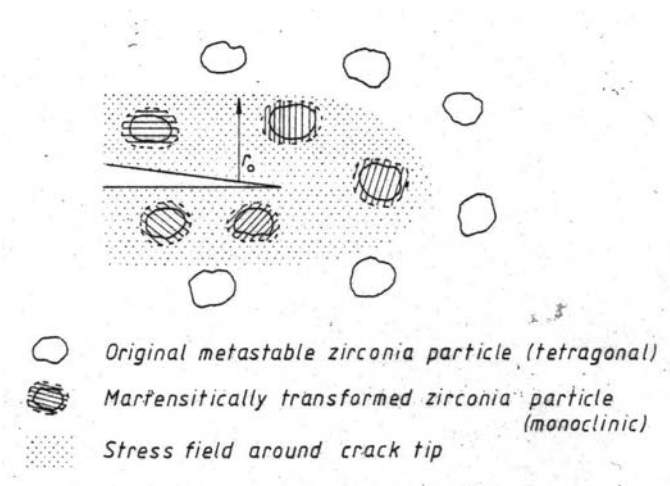


Figure 12: Large tensile stresses generated around a crack can stress induce the tetragonal to monoclinic phase transformation in a process zone around the crack tip. The expansion thus absorbs energy therefore extra work needed to extend crack through the area.

Based on this transformation toughening effect, toughened engineering ceramic has been fabricated as single phase ceramics or dispersing zirconia particles in a ceramic matrix, such as

Al₂O₃, cubic zirconia, etc. These ceramics are commonly used as engineering ceramics such as die inserts.

The low thermal conductivity of zirconia and its excellent chemical resistance enable applications in high temperature environment, such as thermal barrier coating. The basic principle of thermal barrier coating is to apply a thin coating of ceramic over metal components to protect the metal from high temperatures. The zirconia-yttria compositions were found to have high thermal expansion coefficient (to match the nickel based super-alloy), low thermal conductivity and good chemical stability as desired. It can also form an adherent layer with the Ni, Cr, Al, Y bond coat. The most durable coating, consisted of both untransformable tetragonal and cubic zirconia.

Cubic zirconia is also a solid electrolyte. According to calculation the void space available to O²⁻ is larger than that of Zr⁴⁺, thereby it was assumed that O²⁻ ions diffuse faster. Thus, doped cubic ZrO₂ with oxygen vacancies can be used in fuel cells and oxygen sensors:



When there is an oxygen partial pressure difference between the two sides of the solid, O²⁻ ions will diffuse through the electrolyte and an electromotive force (EMF) is generated. The EMF value is related to the partial pressure of oxygen,

$$E = \frac{RT}{4F} \int_{P_{I,O_2}}^{P_{II,O_2}} t d(\ln P_{O_2}) \quad \text{Equation (2.21)}$$

When the ionic conductivity $t_{ion} \approx 1$, the EMF generated becomes

$$E = \frac{RT}{4F} \ln \frac{P_{II,O_2}}{P_{I,O_2}} \quad \text{Equation (2.22)}$$

Thus, cubic zirconia can be used as oxygen sensor or as a solid electrolyte for solid oxide fuel cell (SOFC) as shown in Fig. 13. Fuel passes along one side of the electrolyte and air passing along the other side, giving an oxygen gradient across the sample. The diffusion of O^{2-} ions through zirconia electrolyte allows the oxidation reaction process to continue and generate electrons at anode which are transported through the circuit to the cathode where ionization of oxygen at consume electrons, thereby completing a circuit.

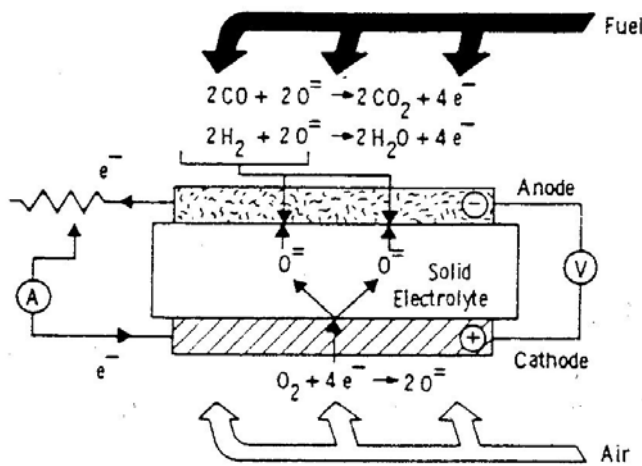


Figure 13: Cubic zirconia used as a solid electrolyte for solid oxide fuel cell.

2.4.2 Hydroxyapatite ($Ca_{10}(PO_4)_6(OH)_2$)

The other system under study here is hydroxyapatite (HA).

Hydroxyapatite exists as monoclinic structure represented by the chemical formula $Ca_{10}(PO_4)_6(OH)_2$. It can also exhibit hexagonal structure. HA powder used to make ceramics is usually chemically synthesized by precipitation from a mixture of calcium nitrate ($Ca(NO_3)_2$) and ammonium dihydrogen orthophosphate ($NH_4H_2PO_4$) solutions. To ensure the purity, commercially bought HA powder is usually calcined at approximately 900 °C before other

processing steps. In addition, attention should be paid to processing temperature since decomposition to tricalcium phosphate can occur at a temperature above 1350 °C.

This compound is found as essential elements in inorganic component of bone and teeth, although the exact structure of biological apatite is not clear.⁴⁴ Thus it is often used as biomaterial, such as bone implants or organ bioreactors.

In particular, HA is biocompatible and bioactive. Since it is bioactive, it will form an interfacial bond with living tissue when in contact with it. Thus in principal, it is an effective repair material. Therefore HA is used in applications such as coatings for metal hip implants to more effectively bond the femoral spick into the leg bone.⁴⁵

2.4.3 α -Alumina

In this study, some images from previous study of α -Al₂O₃ were also used to provide more information.

2.4.3.1 Structure of α -Al₂O₃

α -Al₂O₃ has a typical corundum structure, which is an HCP-based oxide with two thirds of octahedral sites filled. Figure 14 shows a (0001) plane with only one layer of atoms. Oxygen

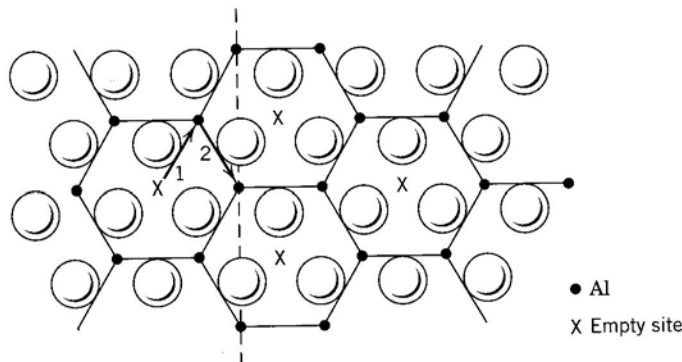


Figure 14: A (0001) plane with only one layer of atoms of typical corundum structure is shown here.

atoms (shown in large empty circles) form a hexagonal array and aluminum atoms (shown in small filled circles) occupy two thirds of the octahedral sites to form a honeycomb configuration. All layers have the same structure except that the second layer is shifted by one atomic space in the direction of 1 indicated in Fig. 14 and the third layer is shifted in the direction of 2 based on

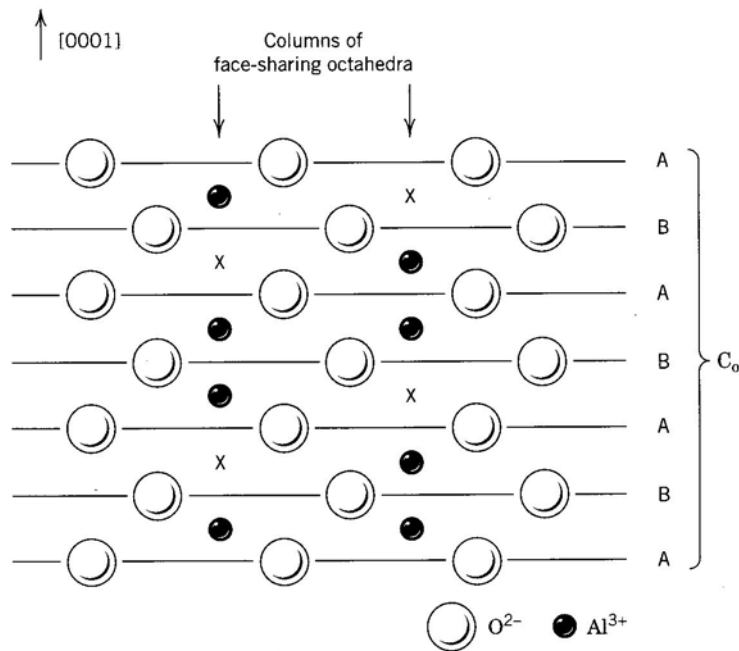


Figure 15: Demonstration of a $\{10\bar{1}0\}$ type plane of a typical corundum structure.

the structure of the second layer. To describe it more clearly, a $\{10\bar{1}0\}$ type plane is demonstrated in Fig 15. The columns of octahedral sites that are perpendicular to (0001) plane alternate in having every two sites occupied and one empty. Figures 14 and 15 show only ideal structures. However, the coulombic repulsion between two adjacent Al³⁺ ions causes each to move slightly toward the empty octahedral site. As a result, the cations form a slight puckered layer, as shown in Fig. 16. Then the oxygen ions also shift slightly from idealized hexagonal close-packed positions. The structure repeats itself every six layers.

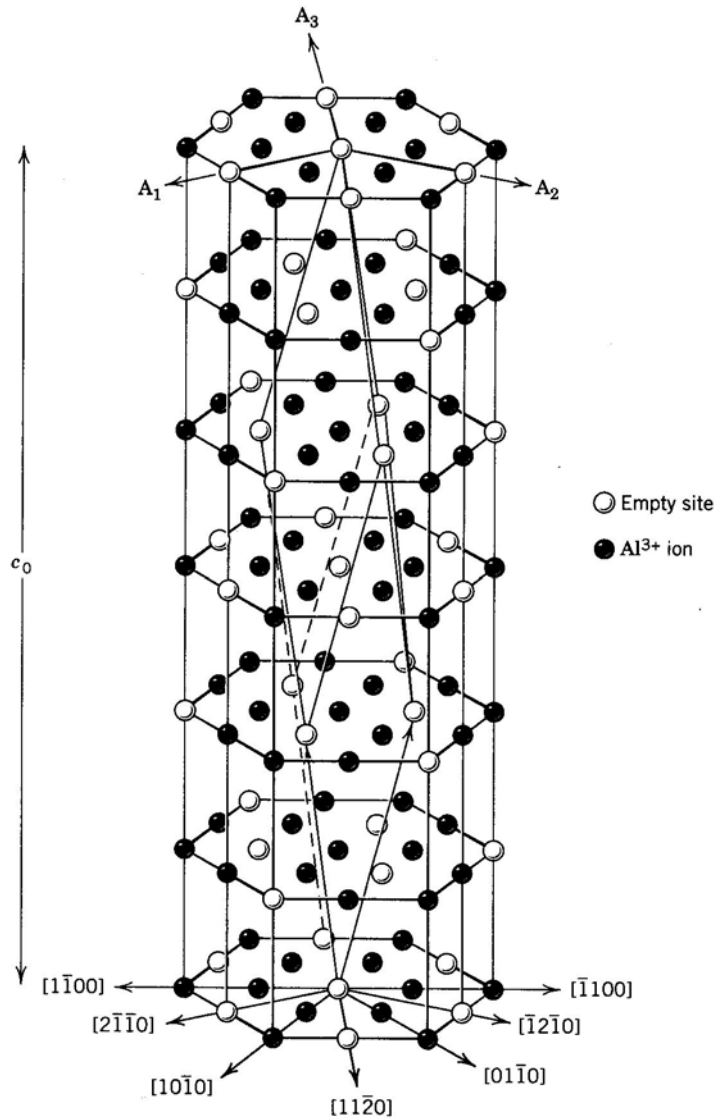


Figure 16: Demonstration of a unit cell of $\alpha\text{-Al}_2\text{O}_3$.

2.4.3.2 Decomposition of $\text{AlO}(\text{OH})$ (Boehmite) to $\alpha\text{-Al}_2\text{O}_3$

A common way to produce $\alpha\text{-Al}_2\text{O}_3$ is starting from Boehmite, which can be easily precipitated by neutralizing aluminum salts or aluminate solutions at temperatures near or above the boiling point of water. Then, the transformation sequence between Boehmite to Corundum involves intermediate Al_2O_3 phases including gamma, delta and theta as shown in Fig. 17. It is important to mention that the transformations from gamma to delta or to theta etc are topotactic

(movement of only cations). The final transformation to alpha is a nucleation and growth of the new hexagonal phase and leads to the loss of a large amount of surface area. Usually the powders must be calcined at 1200C to get phase pure alpha and the powder must be ground. This produces a submicron powder consisting of dense particles containing only a few grains.

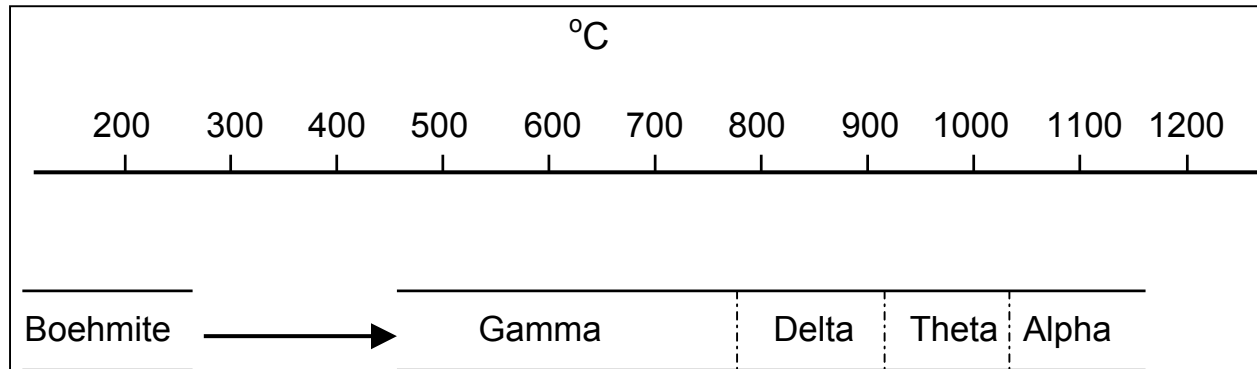


Figure 17: the transformation sequence between Boehmite to Corundum.

2.4.3.3 Property and application of α -Al₂O₃

α -Al₂O₃ possesses variety of good properties, as list in Table 1, which makes it the material of choice for several applications.

Table 1: Properties of 99.5% alumina. ⁴⁶

| 99.5% Aluminum Oxide | | |
|----------------------|-----------------------------|-----------|
| Mechanical | Units of Measure | SI/Metric |
| Density | gm/cc (lb/ft ³) | 3.89 |
| Porosity | % (%) | 0 |
| Color | — | ivory |

Table 1 (continued)

| | | |
|------------------------------------|---|------|
| Flexural Strength | MPa (lb/in ² x10 ³) | 379 |
| Elastic Modulus | GPa (lb/in ² x10 ⁶) | 375 |
| Shear Modulus | GPa (lb/in ² x10 ⁶) | 152 |
| Bulk Modulus | GPa (lb/in ² x10 ⁶) | 228 |
| Poisson's Ratio | — | 0.22 |
| Compressive Strength | MPa (lb/in ² x10 ³) | 2600 |
| Hardness | Kg/mm ² | 1440 |
| Fracture Toughness K _{IC} | MPa·m ^{1/2} | 4 |
| Maximum Use Temperature (no load) | °C (°F) | 1750 |
| Thermal | | |
| Thermal Conductivity | W/m°K (BTU·in/ft ² ·hr·°F) | 35 |
| Coefficient of Thermal Expansion | 10 ⁻⁶ /°C (10 ⁻⁶ /°F) | 8.4 |
| Specific Heat | J/Kg·°K (Btu/lb·°F) | 880 |
| Electrical | | |
| Dielectric Strength | ac-kv/mm (volts/mil) | 16.9 |
| Dielectric Constant | @ 1 MHz | 9.8 |

Table 1 (continued)

| | | |
|--------------------|---------|------------|
| Dissipation Factor | @ 1 kHz | 0.0002 |
| Loss Tangent | @ 1 kHz | — |
| Volume Resistivity | ohm•cm | $>10^{14}$ |

First of all, α -Al₂O₃ is the strongest and stiffest of the oxide ceramics due to the strong ionic interatomic bonding between aluminum and oxygen atoms and the closed packed structure. Thus it is traditionally used as an abrasive or as a component in cutting tools. It can also be used as a refractory material since α -Al₂O₃ has a high melting temperature and resistant to slag in oxidizing environment.

In addition, the electrical resistance of α -Al₂O₃ can be retained up to very high temperatures make it an excellent electrical insulator, too, although the electrical behavior is largely dependent on doping. This electrical insulating behavior enables α -Al₂O₃ to be used in applications such as electrically insulating substrates for electronic circuits.

Last but not least, the optical property of magnesia-doped alumina drew great attentions since the late 1950s. In the absence of magnesia, pores are trapped within large alumina grains and were impossible to remove. Those pores scattered lights and rendered the alumina opaque. The addition of magnesia controlled the grain growth and allowed the removal of pores before they were trapped in the grains. This resulted in transparent alumina that is used as an envelope that contains the plasma in high pressure sodium lamps.

3.0 HYPOTHESIS

It is proposed that an experimentally measured effective diffusion distance can be established for any instant in the sintering process based on the spatial arrangement of pores in real materials. This new experimental parameter should give the expected relationship between densification rate and microstructure parameters and could be used to quantitatively explain the effect of microstructure on sintering kinetics. In particular, the effective diffusion distance would allow simple one dimensional flux models such as the master sintering curve to be used to analyze sintering that starts from different green bodies and provide a means of directly evaluating the effect of powder processing variables on sintering. In short, an experimentally measured effective diffusion distance that is sensitive to the arrangement of pores is needed. This will enable one to deal with a broader range of scenarios for microstructure changes during sintering. After getting that effective diffusion distance, flux can be converted to sintering strain using commonly used cell models, such as that by DeHoff.

4.0 OBJECTIVE

The objective of this study is to measure the effective diffusion distance of different materials and compare the effect of grain size, pore separation and the new effective diffusion distance on volume strain rate. Materials investigated in this study include pressed tetragonal zirconia and hydroxyapatite prepared from aggregated nanocrystalline powders. Images of alumina slip cast using a relatively unaggregated submicron powder were also analyzed. The images were produced by a previous study.

5.0 EXPERIMENTAL PROCEDURE

5.1 SAMPLE PREPARATION

TZ-3YB (ZrO_2 -3mol% Y_2O_3 powder with binder from Tosoh Corporation, Japan) and hydroxyapatite (Sigma-Aldrich) were the materials studied in this work.

5.1.1 Preparation of green bodies

Hydroxyapatite powders were calcined at 900 °C for 30 minutes to ensure phase purity of the materials. These calcined materials were then dried and crushed using a mortar and pestle after they were milled in DI water using zirconia ball for 24 hours.

Both TZ-3YB and HA powders were pressed uniaxially in a 12.9 mm diameter die using a hydraulic laboratory press (Model C-Carver Laboratory Press, Fred S. Carver Inc.). A mixture of stearic acid and ethyl alcohol was coated on the inner surface of die wall as a lubricant. Each sample was pressed from 3 grams of powder. Samples were pressed using a stress of 51 MPa. The bulk density of green bodies was calculated as $\rho = M / V$, where M is the mass and V is the volume. The mass was measured here using Mettler AE200 balance and volume was calculated from dimensions measured using a Mitutoyo caliper gauge.

5.1.2 Sintering

A Lindberg Model 51314 box furnace was used to perform sintering. Green disks were placed on a bed of TZ-3YB or HA powder in a covered alumina crucible (McDanel Refractory Company), which was then placed in the center of the furnace. A typical temperature ramp for sintering is shown in Fig. 18. A heating ramp rate of 5°C per minute and a maximum cooling rate of 10°C per minute were used for all samples during sintering. The peak temperatures for samples TZ-3YB and HA were 1275 and 1100°C respectively.

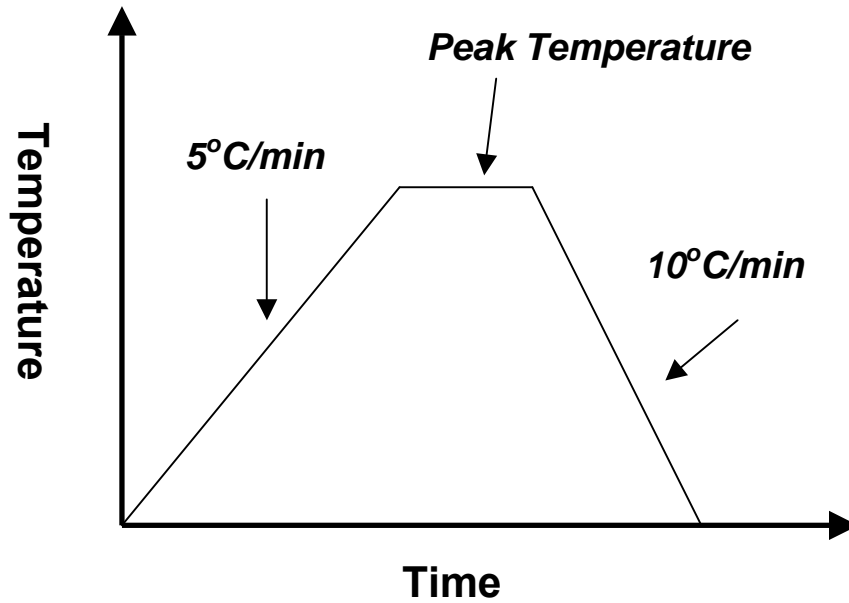


Figure 18: Diagrammatic demonstration for the heating procedure used in this experiment.

Samples were heated at a rate of 5°C per minute to a target temperature, then were held at the peak temperature for a desired time, finally were cooled down at a rate of 10°C per minute to room temperature. TZ-3YB samples were sintered at the peak temperature for 0.1, 0.5, 1, 5, 10 and 50 hours and HA samples were sintered for 0.1, 0.5, 1, 10, 30 and 60 hours respectively.

After sintering, the density of sintered disks was measured based on Archimedes' principle (see Section 5.3.1). These experiments were conducted on more than one sample for each condition.

5.1.3 Sample section and preparation for polishing

Each sintered sample was sectioned parallel to the pressing direction with a diamond saw (Isomet Plus Precision Saw, Buehler Ltd.) in order to expose an inner cross section. After the section, samples were vacuum impregnated with a mixture of resin and hardener (Epo-Thin Low Viscosity Epoxy Resin, Epo-Thin Low Viscosity Epoxy Hardener, Buehler Ltd.) in cold mounting cups. This prevented pull-out during grinding and polishing.

5.1.4 Grinding and polishing

The sectioned surfaces were ground by a Buehler Ecomet 4 Grinder-Polisher plus Automet 2 Power Head with 75 μm and 30 μm diamond wheels before they were polished by the same system with Metadi II Diamond Polishing Compound (Buehler Ltd., 15, 6, and 1 μm diameter diamonds were used). A load of 18 lbs and a speed of 70 rpm were used for the grinding process and the first polishing process with 15 μm diameter diamonds. A reduced load of 17 lbs and speed of 50 rpm were used for the following polishing processes using 6 and 1 μm diameter diamonds. Between different polishing steps, samples were immersed in water and washed in an ultrasonic bath (Branson 5200 Ultrasound). After all grinding and polishing were done, samples were put in an Isotemp Vacuum Oven 282A (Fisher Scientific) to undergo a 10 minutes baking process at 100°C. The purpose of this process is to soften the resin so that the sample could be easily taken out of the mold.

5.1.5 Thermal etching

The polished TZ-3YB samples were thermally etched at 1175°C and HA samples at 1000°C for 0.1 hours to provide grain boundary etching. This step is carried out so that grain boundaries can be better imaged in SEM. The heating rate and cooling rate in the thermal etching process were the same as those used in the sintering process. Densities of samples were measured before and after thermal etching. The results showed that the thermal etching process did not affect the solid volume fraction obtained using Archimedes method.

5.2 MICROSCOPY

To obtain necessary micrographs of those samples, the following steps were used:

(a) A Hummer 10.2 sputtering system (Anatech Ltd, Alexandria, VA) or a Cressington sputter coater, 108 auto/SE (TED, Pella, Inc.) was used to coat a layer of palladium about 5 nm thick onto the etched surface to prevent charging during electron imaging by a scanning electron microscope. Coated samples were stuck onto a metal base and carbon paint was used to establish a conducting path between the metal base and the palladium layer on the samples' surface.

(b) Several images with a digital image size of 712 (width) by 484 (height) pixels were taken on randomly selected regions for each sample surface by using the secondary electron imaging mode of a Philips XL30 FEG SEM. Acceleration voltage and magnifications were chosen to best serve the requirements of analysis (such as grain size and pore size). The other criterion for selecting magnifications is based on a balance between the number of features in an image and the minimum measurable size (number of pixels in each feature).

i) The magnifications used for pore size and pore separation analysis and pore boundary tessellation were 6,250X for TZ-3YB and 5,000X for HA. The magnification factor could vary depending on the solid area fraction of images.

ii) Magnifications used for grain size analysis were 50,000X for TZ-3YB and 2,500X for HA.

5.3 DATA ANALYSIS

Necessary parameters needed to represent those samples were bulk density, apparent density, densification rate, pore separation, grain size, solid area fraction, the number of pores per unit area, and the effective diffusion distance, etc. This section describes the procedures to obtain these parameters.

5.3.1 Measurement of densities

Bulk density and apparent density were investigated using the Archimedes method. The mass of each sample was measured while the sample was dry, which was denoted as M_d . After that, the sample was placed inside a vacuum system along with a bowl of distilled water. The vacuum system was then pumped by a mechanical pump to drive air from pores of the sample. After several minutes pumping, the sample was dropped into the water bowl and stayed there for about 15 hours to allow water to flow into all the pores. After the 15 hours of soaking, the mass of the sample was measured again under two different settings. The suspended weight (denoted as M_s) was measured while the sample was still immersed in water and an underwater supporting

platform was used to suspend the sample under the balance. The other mass (denoted as M_i) was measured immediately after sample was taken out of water (at this time, the sample was still saturated with water). The bulk density and the apparent density were expressed below, where ρ_{theo} is the theoretical density (here the value $\rho_{theo} = 6.05, 3.98$ and 3.16 g/cm were used for TZ-3YB, alumina and HA, respectively), ρ_{water} was theoretical density of water (here the value $\rho_{water} = 1$ g/cm was used).

$$\rho_{bulk} = \frac{M_d \rho_{water}}{(M_i - M_s) \rho_{theo}} \quad \text{Equation (5.1)}$$

$$\rho_{app} = \frac{M_d \rho_{water}}{(M_d - M_s) \rho_{theo}} \quad \text{Equation (5.2)}$$

5.3.2 Calculation of isothermal densification rate

Plots of solid volume fraction versus log time in hours were made. Equation (5.3) was used to calculate densification rate during isothermal sintering. The rate constant a was obtained as the slope of the plot of solid volume fraction versus log time in hours, ρ_1 was the relative density at a time of 1 hour, and ρ was the solid volume fraction at time t .

$$\frac{d\rho}{dt} = a \exp\left(\frac{\rho_1 - \rho}{a}\right) \quad \text{Equation (5.3)}$$

5.3.3 Measurement of average pore separation and grain size

Average pore separation and grain size were measured from those SEM images obtained in Section 5.2. Parallel test lines were drawn horizontally on each image taken at randomly

picked locations. The number of two kinds of intersection points, i.e. solid-vapor interface and solid-solid interface were counted. The fractional length of test line through the pore phase L_L^P was measured. L_L^S (Solid length fraction) was calculated and was compared with bulk density of the sample, where L was the whole length of each line and N was the number of lines on each image.

$$L_L^S = 1 - \frac{\sum L_L^P}{L \cdot N} \quad \text{Equation (5.4)}$$

Then $V_V^P \approx L_L^P$ under the assumption that the images are representative of whole sample.

The number of solid-vapor interface intersection points per unit length on each line was defined as P_L^{SV} and the number of solid-solid interface intersection points per unit length was defined as P_L^{SS} . Therefore, the surface area per unit volume of pore surface S_V^{SV} and grain boundary S_V^{SS} can be calculated using

$$S_V = 2P_L \quad \text{Equation (5.5)}$$

Thus, assuming all pores are located on grain boundaries, the equation for determining average grain intercept length (average distance in the solid phase between any types of boundary) is as follows: ^{47,48,49,50,51}

$$\lambda_g = \frac{4L_L^S}{S_V^{SV} + 2S_V^{SS}} \quad \text{Equation (5.6)}$$

The equation for determining average pore separation (average distance in the solid between pore boundaries) is:

$$\lambda_{PS} = \frac{4L_L^S}{S_V^{SV}} \quad \text{Equation (5.7)}$$

The pore intercept size can be calculated from Equation (3.8):

$$\lambda_p = \frac{4(1 - L_L^S)}{S_V^{SV}} \quad \text{Equation (5.8)}$$

5.3.4 Analysis of solid area fraction and number of pores per unit area

Solid area fractions and number of pores per unit area were measured by using a digital micrographs software named ScionImage to create binary (black and white) images. Images taken of the sample using SEM were first duplicated. Changes were only made in the duplicated

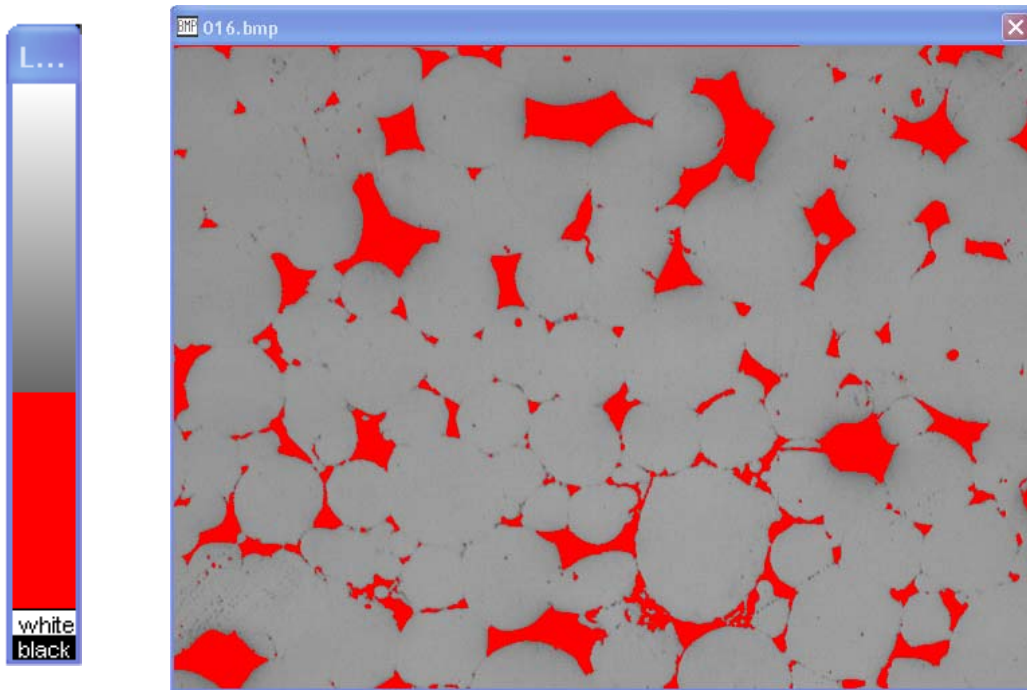


Figure 19: Showing the density slice operation in which the top line in left toolbar is dragged to adjust the contrast of image when “Density Slice” command was performed.

copy. Noise was reduced by using a command “Rank Filters/ Median” as the first step. A command “Density Slice” (Fig. 19) was performed while comparing the duplicated copy with the original image before it was saved as a binary image. Some manual completion of pores needs to be performed for each micrograph.

After software processing, Fig. 20 shows that the pores were presented as black features while solid area was shown as white in the images. Solid area fraction was then the percentage of white pixels in the image, which can be obtained by performing “Threshold” and “Show Results” commands in the software. Solid area fraction obtained using this method could be compared with the solid volume fraction obtained from the Archimedes method in order to verify that a statistically significant number of micrographs have been used in the analysis. A 95% confidence interval was considered appropriate for the solid area fraction obtained by this software. Then the number of feature per unit area can be counted and the pore size distributions constructed.

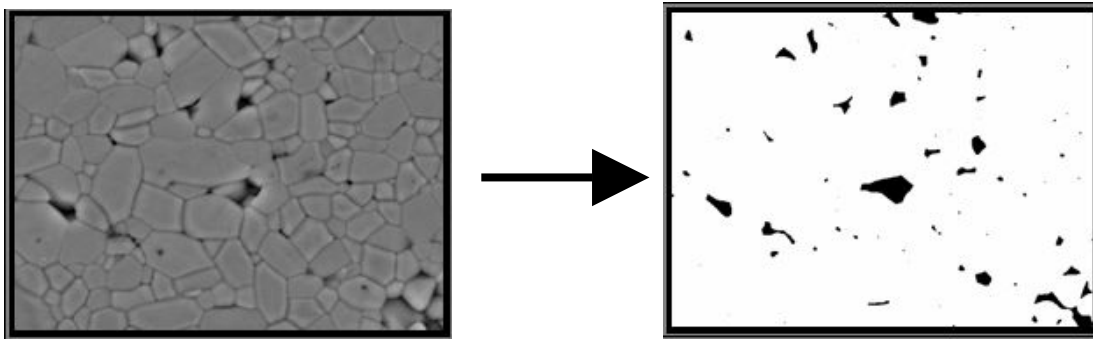


Figure 20: The original SEM image (left) and the binary image converted from it by software “ScionImage” (right).¹⁹

5.3.5 Measurement of effective diffusion distance in the proposed work

Binary images have to be obtained prior to running the Tessellator program. Any object that was smaller than 2 pixels were filtered thus very small pore features will be omitted although it is thought that the number of those very small pore features was not significant. Tessellation cell maps were created by processing those binary images. The way one constructs a tessellation cell in this study is like constructing a Voronoi polyhedron outside of pore

boundaries in two dimensions. As shown schematically in Fig. 21, a tessellation cell contains the central pore and fractions of the surrounding grains. Additionally, when the tessellation

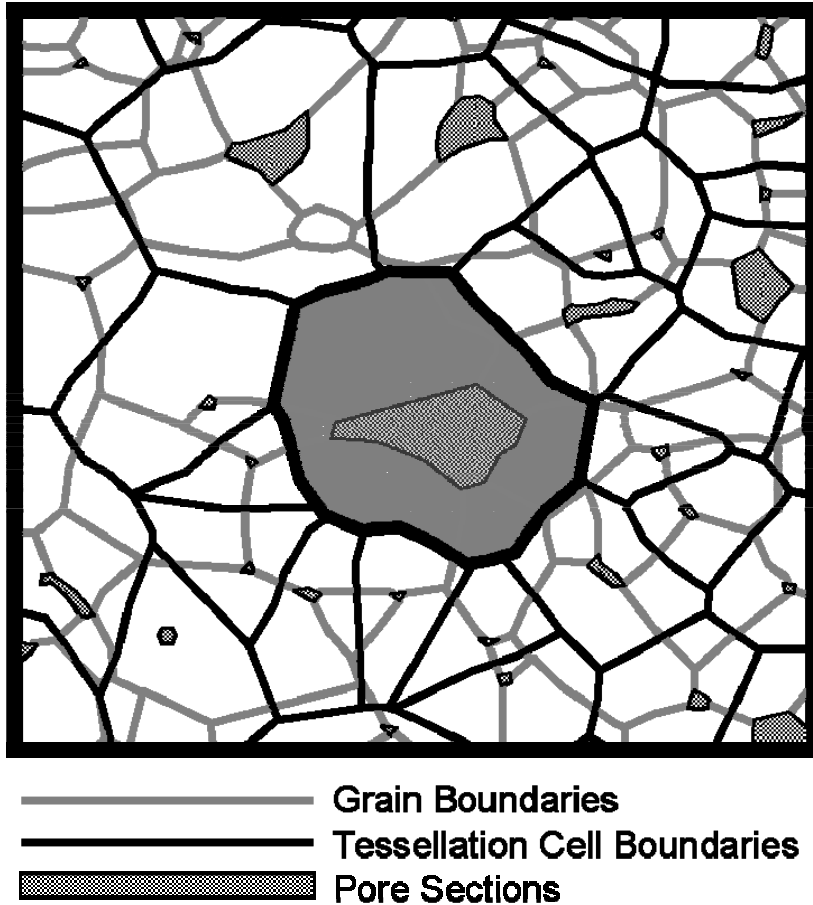


Figure 21: The illustration of pore boundary tessellation.

technique is repeated it always gives a unique segmentation of the microstructure. The size and shape of the tessellation cells are sensitive to the local arrangements of pores and the pore sizes.

A distance map could be prepared from the binary pore image by correlating the grey scale of a pixel in the solid to the distance from the pore boundary. One example of a distance map is shown in Fig. 22(a). In this case, the distance map selects gray scale values of the tessellation boundaries based on a normalized square of the distance to the nearest pore boundary. The further away from a pore the pixel is the darker the grey scale. The effective

diffusion distance λ_{di} for the central pore in that cell can then be calculated by superimposing a pore boundary tessellation and determining the grey scale of the pixels on the cell boundary. By averaging the values for all the cells in the images, the average effective diffusion distance λ_d for the area being studied can be determined.

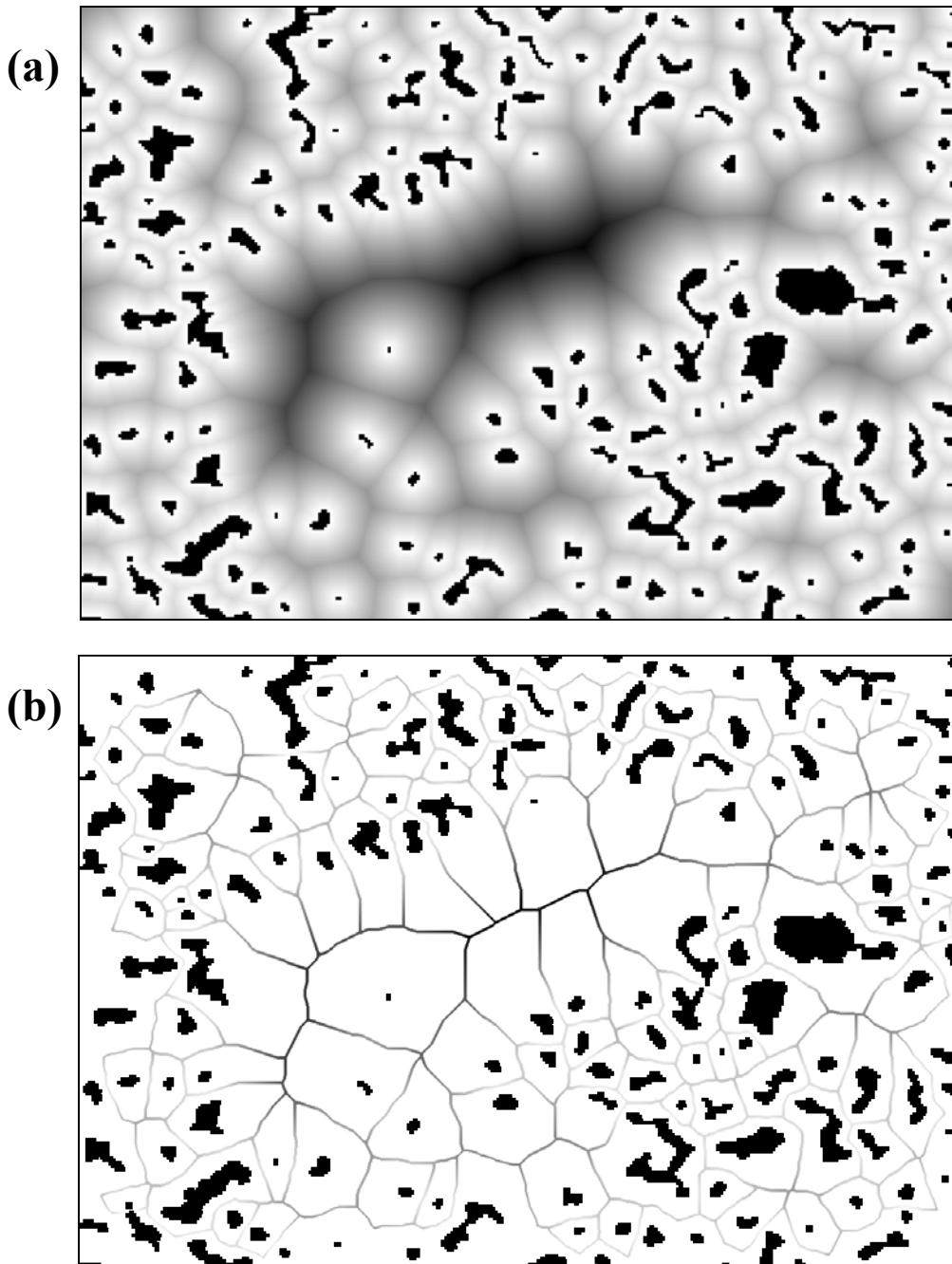


Figure 22: An example of distance map obtained from tessellator.

6.0 RESULTS AND DISCUSSION

6.1 DENSIFICATION

Isothermal sintering curves were obtained for $\text{ZrO}_2\text{-3mol\%Y}_2\text{O}_3$ (TZ-3YB) sintered at 1275°C and hydroxyapatite (HA) sintered at 1100°C are shown in figures 23 and 24. The solid triangles represent the bulk density of TZ-3YB, while the hollow triangles represent the apparent density of TZ-3YB. Similarly, solid circles represent the bulk density of HA, and crosses represent the apparent density of HA.

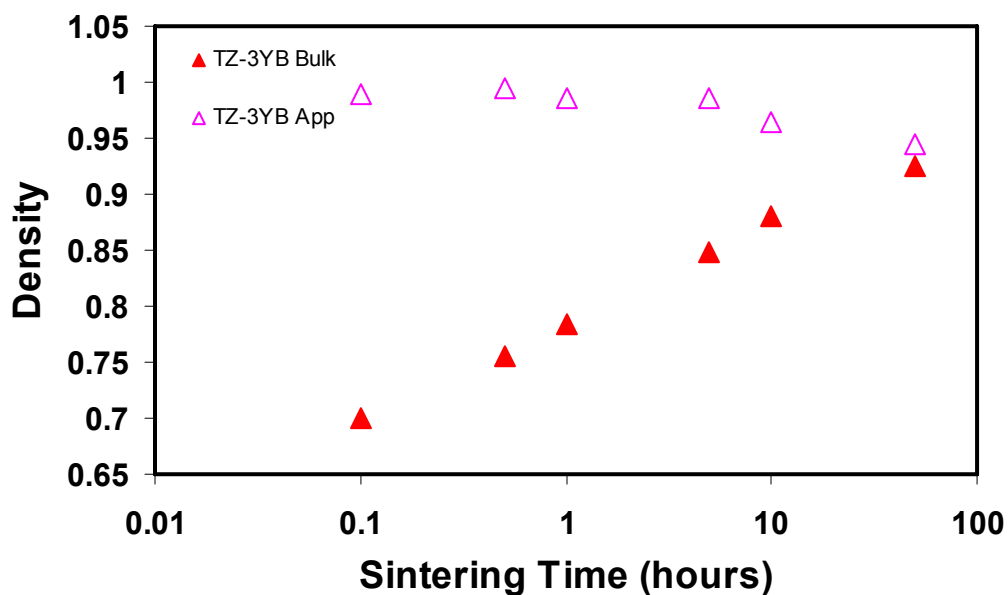


Figure 23: The effect of sintering time on solid volume fraction of $\text{ZrO}_2\text{-3mol\%Y}_2\text{O}_3$.

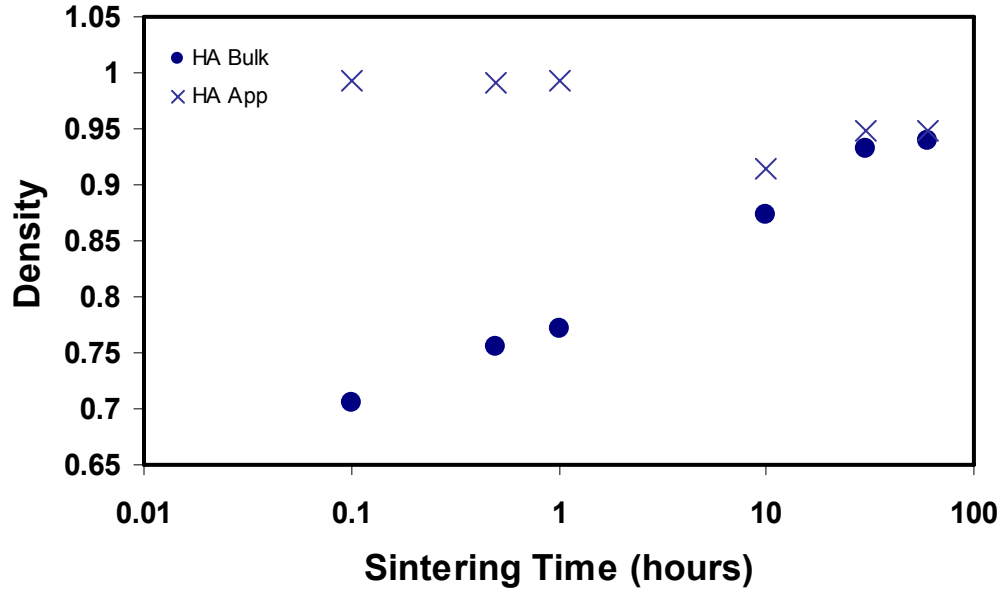


Figure 24: The effect of sintering time on solid volume fraction of hydroxyapatite.

The expected semi-log dependence behavior of solid volume fraction (bulk density) on sintering time, was seen for both ceramics. In other words, the sintering kinetics follows the equation shown below:

$$\rho = \rho_0 + K \ln t \quad \text{Equation (6.1)}$$

Where ρ is the solid volume fraction (SVF) after isothermal sintering for a period of time t . ρ_0 is the SVF after isothermal sintering for 1 hour. K is a constant. K could be viewed as the slopes of curves in a SVF- $\ln(\text{time})$ graph. After fitting experimental data shown in figures 23 and 24 by using Equ. 6.1, parameters ρ_0 and K can be deduced. In our experiments, data from TZ-3YB samples fits the equation $\rho = 0.7854 + 0.0373\ln(t)$, the slopes was $0.0373 [\lg(\text{hours})]^{-1}$. Similar observation for HA and data from HA samples fits equation $\rho = 0.785 + 0.0391\ln(t)$ with a slope of $0.0391 [\lg(\text{hours})]^{-1}$.

The SVF (solid volume fraction) of TZ-3YB sample increased from the green density of 0.45 to 0.70 after being heated using a rate of $5^\circ\text{C}/\text{min}$ to 1275°C and held at that temperature for

0.1 hours. Similarly, the SVF of HA increased from the green density of 0.46 to 0.71 after 0.1 hours sintering at a temperature of 1100 °C. In both materials approximately 50% of the pore volume in the sample was removed during this procedure. However, after 50 hours holding at 1275°C, the bulk density and apparent density of TZ-3YB sample were 0.923 and 0.944. A significant difference of 0.021 between these two densities still existed, which indicated that some of the pores in this sample were connected to the surface. Similar results are found for HA, after 30 hours of sintering. By comparing the bulk densities and the apparent densities it can be concluded that initially all the pores are open for both materials but at a solid volume fraction of approximately 0.9, the pores begin to close and they are all closed by the time solid volume fraction reaches approximately 0.95. This is commonly observed in solid state sintering of ceramics.

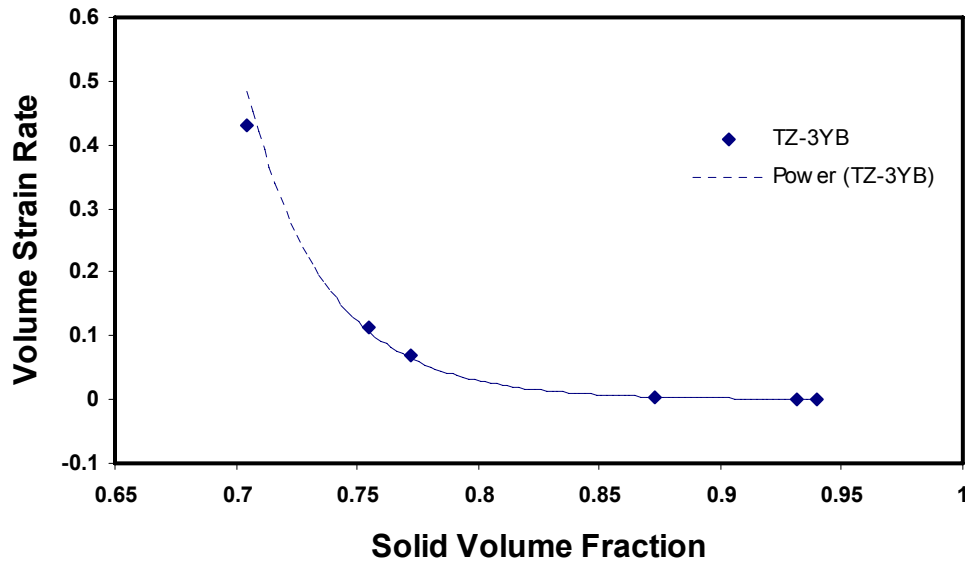


Figure 25: The relationship for isothermal sintering of TZ-3YB between Volume Strain Rate and Solid Volume Fraction. The dash blue curve is power fitting of data points.

The volume strain rate can be determined by differentiating the experimentally fitted equations for data shown in figures 23 and 24. The plot of volume strain rate $[dp/(pdt)]$ v.s. Solid

Volume Fraction is shown in figures 25 and 26 for both TZ-3Y and HA. As exhibited in this graph, densification rates for zirconia (0.0008) and HA (0.0009) samples do not reach zero after the longest sintering time used in our experiments, suggesting that not all sintering was exhausted.

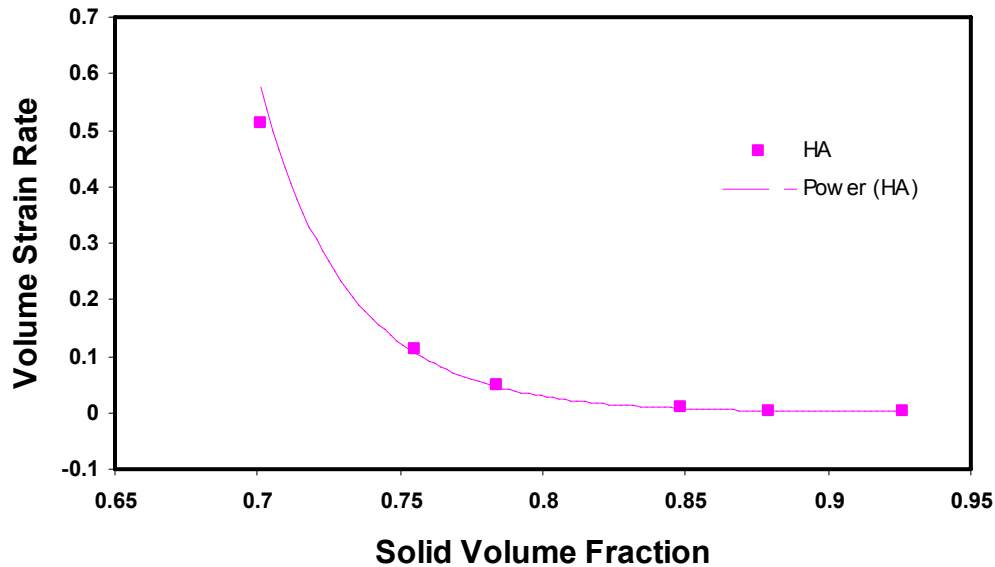


Figure 26: The relationship for isothermal sintering of HA between Volume Strain Rate and Solid Volume Fraction. The dash pink curve is power fitting of data points.

6.2 GRAIN INTERCEPT, PORE SIZE AND PORE SEPARATION

The effect of green density on sintering behavior of ceramics has been reported previously.^{30, 31} In general, the effect is thought to be that the wide pore size distribution associated with low green density affect coarsening of the grain structure (wider distributions tend to drive coarsening or ripening processes more) and coarsening increases the separation of sinks for diffusion and decreases the densification rate. Thus, it was necessary to obtain certain microstructure results such as average grain size, pore size and pore separation in this study in

order to determine if the observed effect of density on densification rate is associated with coarsening of the pores and grains. Previous studies have shown that this system (ZrO_2 -3mol% Y_2O_3) exhibits densification by grain boundary diffusion⁵² and a $1/\lambda_g^3$ dependence of densification rate is thus expected.⁵³ Therefore based on these expectations, coarsening of the grain structure should have a dramatic effect on densification rate.

Average grain intercept length, average pore intercept length and average pore separation intercept length (as defined in section 5.3.3) were measured from SEM images, characterizing the average size of the grains, pores and the average separation between adjacent pores respectively. The measured dependence of grain size and pore size on solid volume fraction is shown in Fig. 27. All error bars in this study are calculated as the 95% CI between the images. Equation 6.2 is used to obtain the value of the error bar, where σ is the standard deviation for a pool of values obtained from individual images and N is the number of images analyzed.

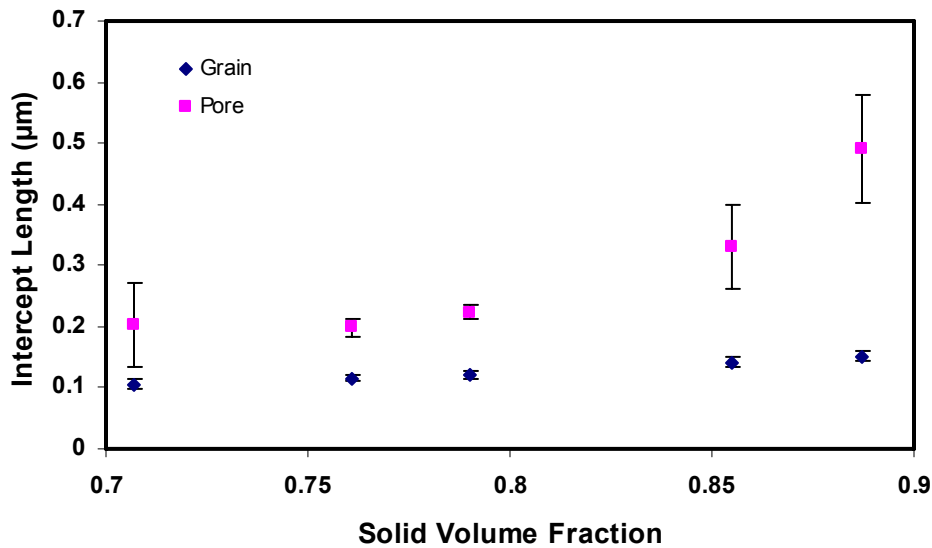


Figure 27: The average grain and pore intercept length plotted against solid volume fraction for TZ-3YB samples.

$$95\%CI = \frac{2 \cdot \sigma}{\sqrt{N}}$$

Equation (6.2)

As shown in Fig. 27, the average grain intercept length of TZ-3YB is 0.1 μm at a solid volume fraction of 0.71 and then increases slowly to 0.15 μm at a solid volume fraction value of 0.88 after 10 hours sintering. The slow increase agrees with previous results in literature ⁵⁴ that suggest grain growth is very slow in this system. Also, over the same range of solid volume fraction the average pore size intercept length increased from 0.20 to 0.49 μm . The increase of average intercept length of pores is slightly greater than that of grains. Traditional models of sintering assume pores exist in every grain edges. In contrast, we observed that the pore separation is greater than grain size, which does not consistent with the assumption of traditional models but instead suggests pores are large and must be separated by more than one grain.

In contrast to those small changes in pore size and grain size, we observed a considerably larger increase in the pore separation. (Fig. 28) The pore separation increased from 0.49 μm to

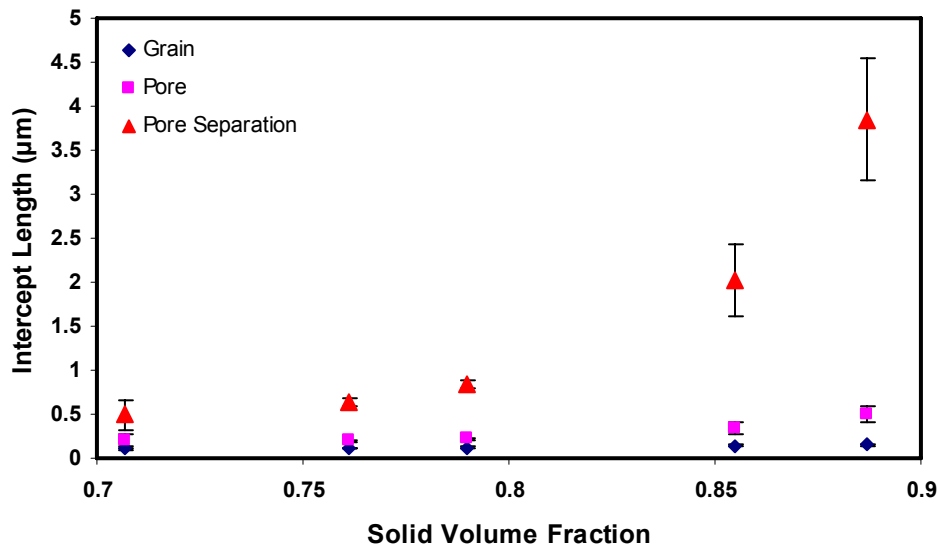


Figure 28: The average grain, pore and pore separation intercept length plotted against solid volume fraction for TZ-3YB samples.

3.85 μm over the same range of solid volume fraction mentioned above. As seen in Fig. 29, the ratio of pore separation (3.85 μm) to average grain intercept length (0.15 μm) was more than 25 at a solid volume fraction value of 0.89, which was much greater than the value of 4.7 when the solid volume fraction was 0.71. This suggests that the pore separation is increasing faster than the grains and grain coarsening alone cannot be responsible for the increase in pore separation as implicitly assumed by the sintering models.

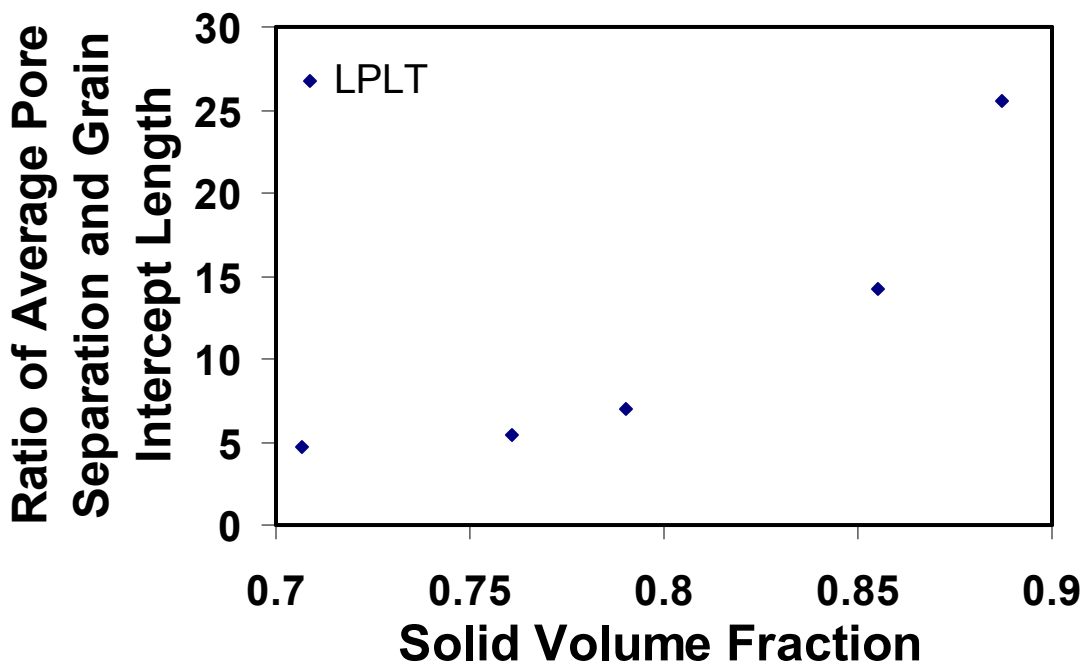


Figure 29: Plot of Ratio of average pore separation intercept length and grain intercept length against Solid Volume Fraction of TZ-3YB samples.

The slope of linear trend line with log volume strain rate against log inverse intercept length of these zirconia samples was shown in Fig. 30. As seen in Fig. 30, the slope for grain size is 12.9 which is much higher than 3, the expected value based on some previous study suggesting this zirconia material densifies via volume diffusion. This indicates that the decrease in densification rate during isothermal sintering cannot be explained by the increase in grain size

alone. Again this violates the implicit assumption in equation 2.21. Some other process must also be contributing to the increase in diffusion length during isothermal sintering. In contrast, the slope of pore separation has a value of 2.2 which is closer to the expected value of 3. However, for the pore separation data, the slope between each two contiguous data points decreased from 5.91, 2.66, 1.98 to 1.31, respectively, as the densities of samples increasing. This result suggests that the inter pore distance can scale the diffusion length to the model better than grain size does. However, the power law relationship does not fit the data well.

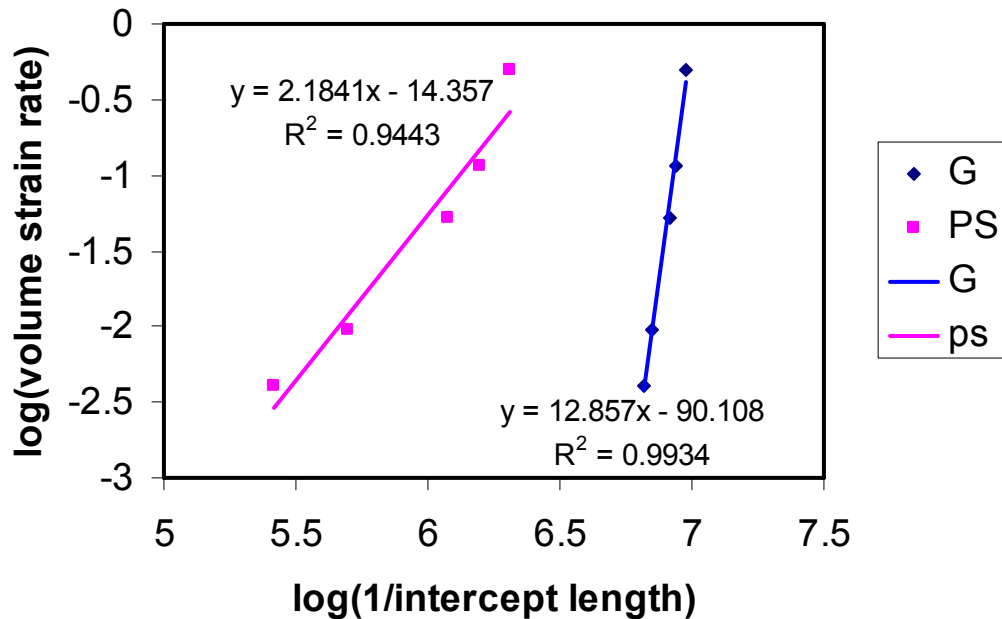


Figure 30: Plot of log volume strain rate against log inverse intercept length (grain and pore separation) of TZ-3YB.

Similarly, in the case of HA, when sintering progresses, we also observed a considerably larger increase in the pore separation than in grain and pore sizes, as shown in Fig. 31. The slope of linear trend line with log volume strain rate against log inverse intercept length of HA samples was shown in Fig. 32. For this system, the slope for the grain intercept is 6.74 and that of the pore separation is 2.02.

To compare the results obtained with TZ-3YB and HA with results for a ceramic made from a relatively unaggregated powder, some results from a previous study on alumina were

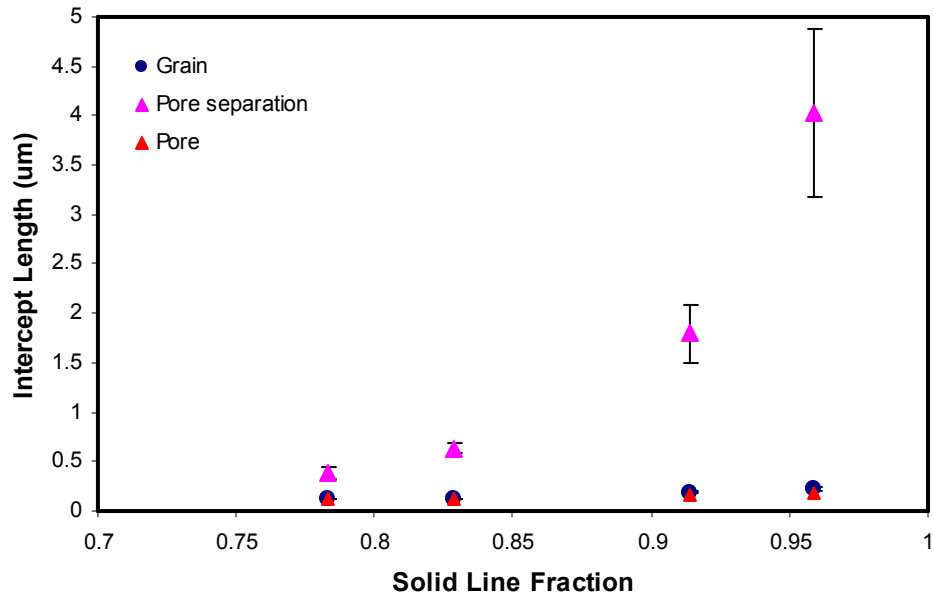


Figure 31: The average grain, pore and pore separation intercept length plotted against solid volume fraction for HA samples.

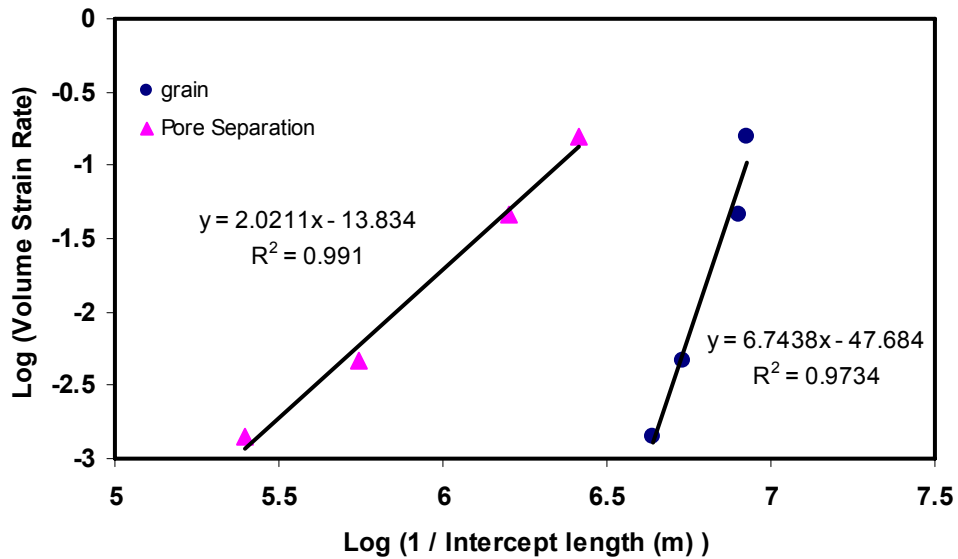


Figure 32: Plot of log volume strain rate against log inverse intercept length (grain and pore separation) of HA.

considered. In the previous study samples were made from a commercial alumina powder resulting in a much higher bulk green density of 0.57 (much higher than those of samples in this study) after dry pressing. This material gave a much lower ratio of grain size to pore separation during sintering than the TZ-3YB samples and HA studied here.⁵⁵ After 10 hours sintering, that alumina has a pore separation to grain intercept ratio of less than 8 at a solid volume fraction of 0.96, which is much smaller than the ratios of TZ-3YB and HA, as shown in Fig. 33. This

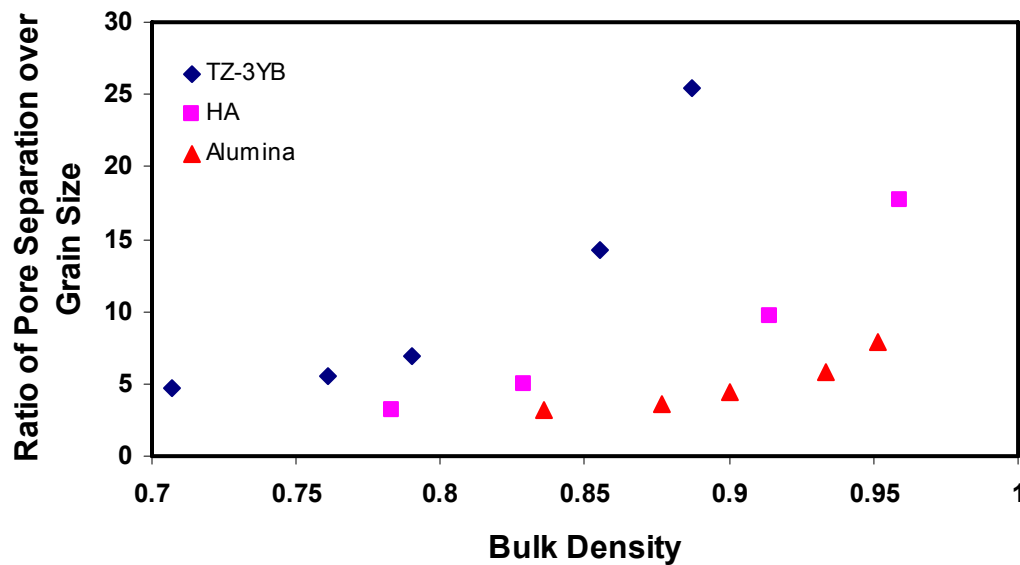


Figure 33: Comparison of Ratios of average pore separation intercept length over grain intercept length as isothermal sintering time increase among TZ-3YB, HA and dispersed alumina samples.

previous study with commercial alumina powder also showed that the number of pores per unit area did not decrease much below a solid volume fraction of 0.9 and agrees with the common expectation, reflected in the models of sintering, that pore elimination does not begin to affect the results until pores pinch off and become isolated in the very last stage of final stage of sintering. Instead, the number of pores per unit area of TZ-3YB (shown in Fig. 34) decreases rapidly as isothermal sintering time increase before solid volume fraction reaches 0.9. This

suggests that in TZ-3YB system pore channels must be shrinking along their length or pinching off during intermediate stage of sintering and this behavior would lead to an increase in the effective diffusion distance.

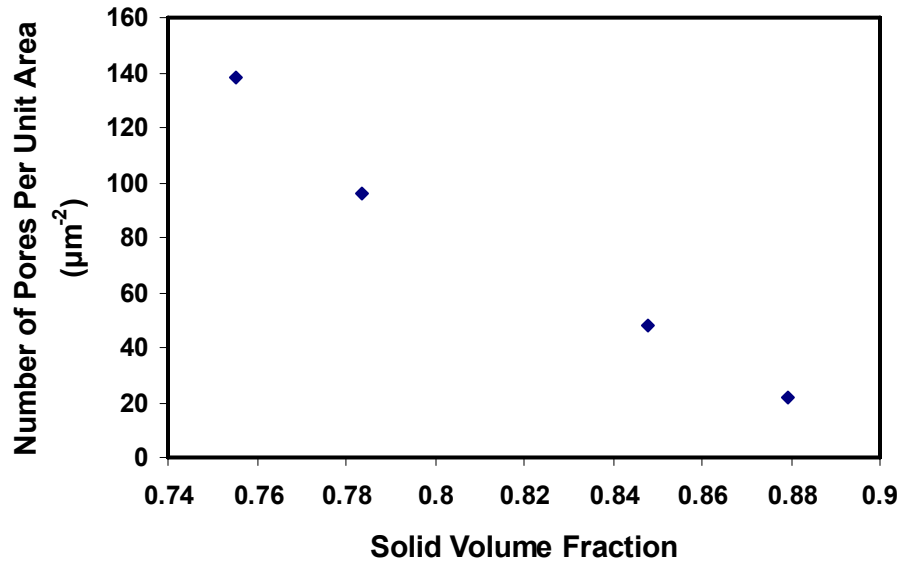


Figure 34: Number of pores per unit area of TZ-3YB decrease rapidly as isothermal sintering time increases.

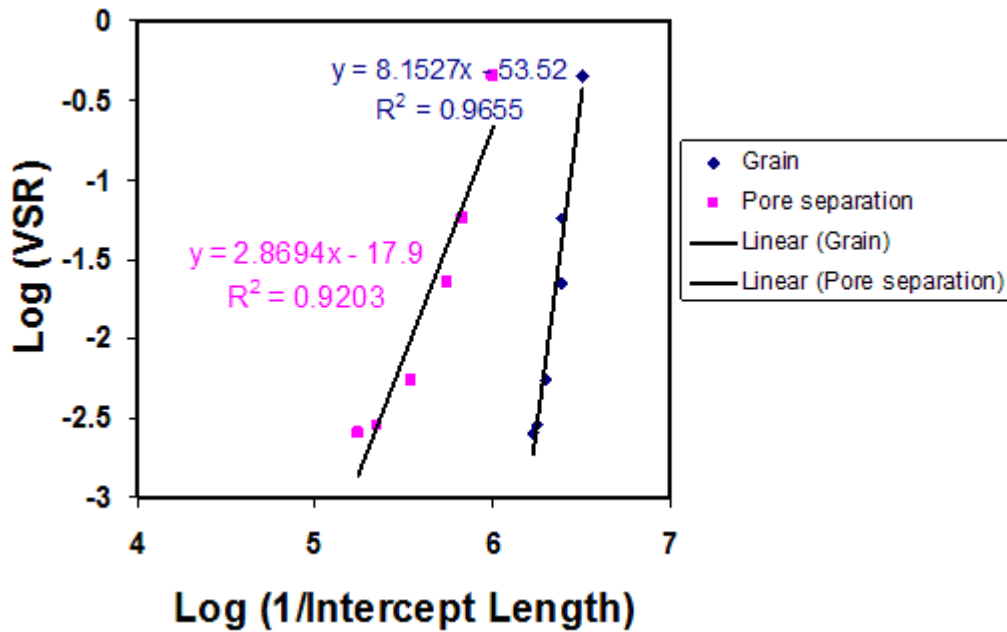


Figure 35: Plot of log volume strain rate against log inverse intercept length (grain and pore separation) of dispersed alumina samples.

The slope of linear trend line with log volume strain rate against log inverse intercept length of those alumina samples shown in Fig. 35 also suggests that inter-pore distance can be a better parameter to scale the diffusion length to the model than grain size, since the slope of pore separation is 2.9, which is closer to 4 again than the value of 8.2 for measured for grain size. The commonly accepted correlation between the diffusion length for the dominant mass transport mechanism and grain size are based on the sintering models that assume pores exist on all grain edges during intermediate stage of sintering or on all grain corners during final sintering stage. If this assumption was correct, there would be no difference in the ratio of grain intercept to pore separation between alumina, HA and zirconia. This assumption appears not to be true in our case, since the average separation of pores we observed is much larger than the grain size. In addition, as shown in Fig. 36, pores were not observed in triple-point in this zirconia material when the SEM pixel resolution is about 7 nanometers.

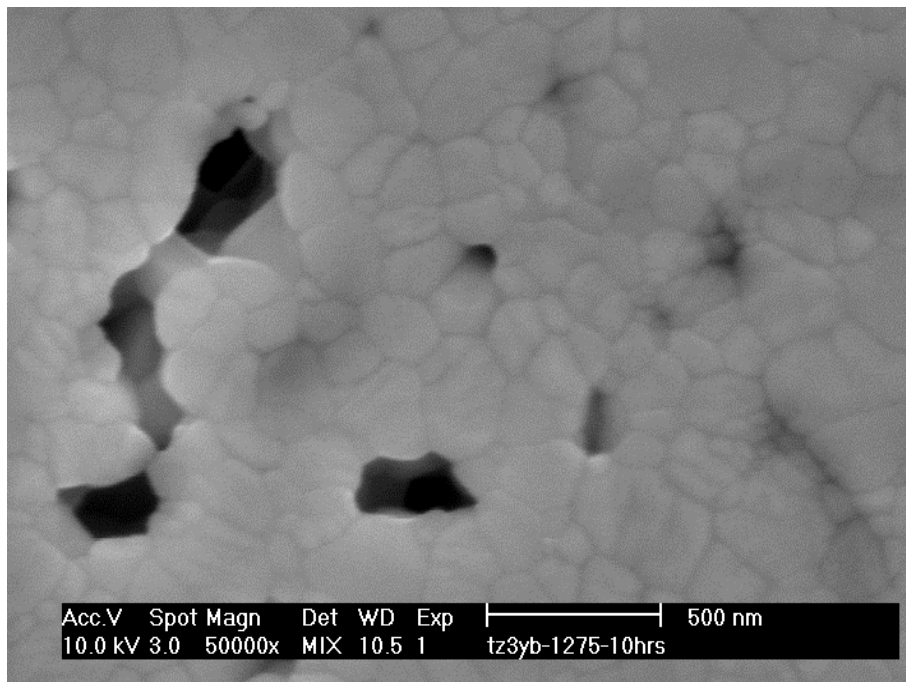


Figure 36: A high magnification SEM image shows there is no vacancy in triple point in the polished cross-section of these zirconia ceramics.

It is important to know whether or not our measured results are representative since it is possible that very fine pores, below the pixel resolution are being eliminated from the analysis. This was tested for samples TZ-3YB which is the ceramic with the finest pores. The measured area fraction A_A of pores from the analysis of images were found to be about the same with the solid volume fraction measured from the Archimedes method, which means the SEM images taken in these locations can represent the whole material at least in terms of pore volume. The solid area fractions of those SEM images measured by the software Scion Image were 0.78, 0.82, 0.87 and 0.93 for 0.5 hours, 1 hour, 5 hours and 10 hours of sintering at 1275 °C respectively, which were very close to but slightly higher than V_v measured by Archimedes method of 0.76, 0.79, 0.86 and 0.89. Similar results are found for the HA in this study. The densities measured by Archimedes (V_v) and by two dimensional images (A_A) of these two systems are listed in Table 2. This suggests no statistically relevant population of small pores was missed in our measurements. It is of course possible that a few small pores were missed but they were not statistically significant. In summary, the above discussions suggest that for the zirconia samples and HA samples studied here, grain intercept length did not relate to the diffusion length in the way assumed by the existing sintering models and all the interpretation of experimental results associated with them. This is because the pore separation is larger than the grain size at any particular solid volume fraction and increases faster with sintering. However, pore separation measured in this material could correlate more strongly with diffusion length than the grain size and it suggests that pore separation is a better representation of the microstructural scale in sintering contrary to the assumption of microstructure maps which only use grain size to represent microstructural scale.^{56,22} The observations made here may not be general to ceramics

sintered at higher temperatures because of very slow grain growth at the comparatively low sintering temperatures of this study.

Table 2: Comparisons of densities measured by Archimedes and images

| | Archimedes Density (V_v) | Solid Area Fraction by images (A_A) | Difference |
|----------------|------------------------------|---|------------|
| TZ-3YB 0.5 hrs | 0.76 | 0.78 | 0.02 |
| TZ-3YB 1 hrs | 0.79 | 0.82 | 0.03 |
| TZ-3YB 5 hrs | 0.86 | 0.87 | 0.01 |
| TZ-3YB 10 hrs | 0.89 | 0.93 | 0.04 |
| HA 0.5 hrs | 0.75 | 0.78 | 0.03 |
| HA 1 hrs | 0.77 | 0.83 | 0.06 |
| HA 10 hrs | 0.87 | 0.91 | 0.04 |
| HA 30 hrs | 0.93 | 0.96 | 0.03 |

To account for the microstructures observed in this study, Fig. 37 shows a new conceptual model that does not require pore channels on every grain edge (triple point) during sintering as required by the existing phenomenological models. All of previous sintering models require uniformly distributed vacancy annihilation along grain boundaries with pores separated by only one grain boundary. Fig. 37 illustrates how the proposed mechanism employs diffusional creep to allow uniform distribution of vacancy annihilation along the grain boundaries with more than one grain in the unit cell. In Fig. 37, the vacancy annihilation along grain boundary between Grain 1 and Grain 2 would create tension on boundaries between Grain 1 and Grain 3 and between Grain 2 and Grain 3. This would drive vacancy diffusion along these boundaries and consequent vacancy annihilation. Therefore it is possible to have more than one grain in a unit cell as long as there is uniform annihilation of vacancies along all grain boundaries. Thus grain

boundary diffusion would result in the necessary creep and densification. However, the diffusion length is correlated with the average pore separation, not with the grain size. This conceptual model would lead to the conclusion that coarsening in this study, as reflected in the pore separation length, is occurring much more quickly than one would expect from the grain size plotted in Fig. 28. This enhanced coarsening is therefore responsible for the decrease in densification rate and the inability of grain size to account for the decrease in densification rate.

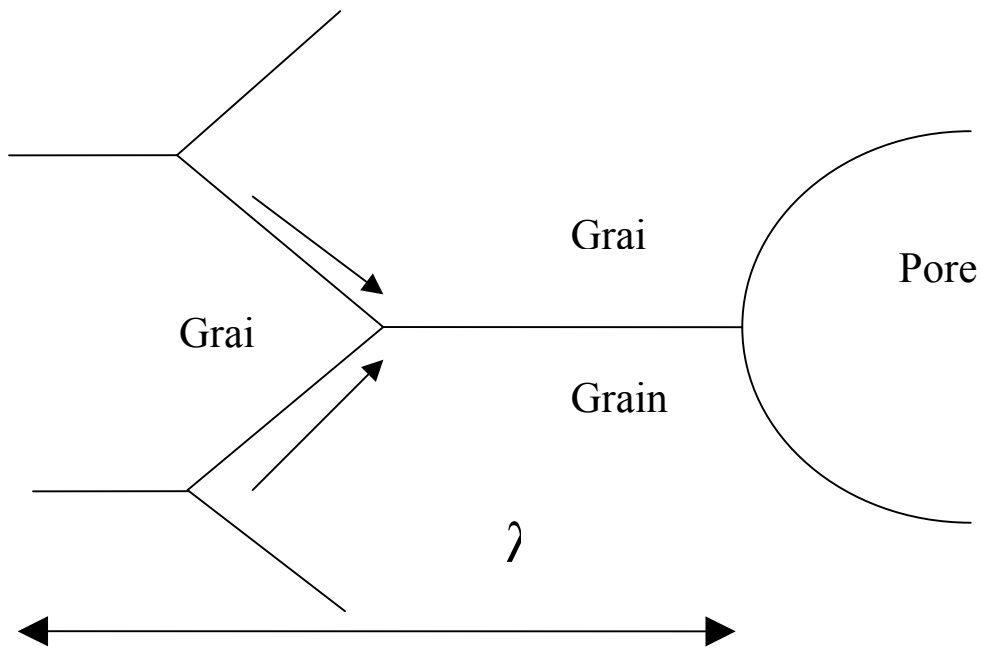


Figure 37: A two dimensional representation of a microstructure with more than one grain between pores. Vacancy annihilation on boundary between grain 1 and grain 2 would create tension without mass transport along boundaries between grain 1 and grain 3 and boundaries between grain 2 and grain 3 in response to stress.

However, as described earlier, the pore separation does not fit the functional form very well for TZ-3YB and the slope of the pore separation data decreased and became far from a value of four as the density of samples increased. This result showed that the pore separation may represent the diffusion length well in low density samples while in high density samples the

pore separation result seemed to overestimate the diffusion length based on the expected exponent. One possible reason for this discrepancy between samples with different density values is the different pore arrangements in those samples. From SEM observation (see Fig. 38),

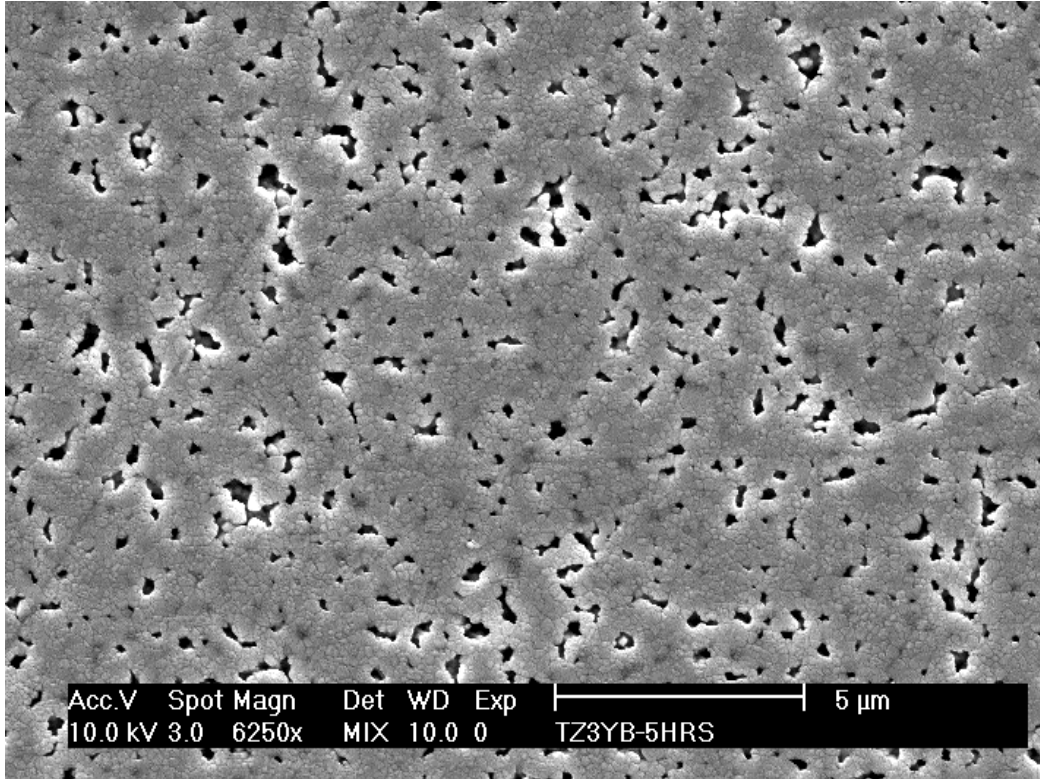


Figure 38: The non-random pore arrangement by in TZ-3YB samples SEM observation. Pores appear to reside more at the boundaries of dense regions containing many grains as schematically.

we found that the pore arrangement in this material showed a non-random (preferential) arrangement in which pores appear to reside more at the boundaries of dense regions containing many grains as schematically shown in Fig. 39. In order to describe this structure better, we called those dense areas “cores” and those relatively porous areas between them “shells”. As the isothermal sintering time increase, the individual core areas grow in size and the porous areas

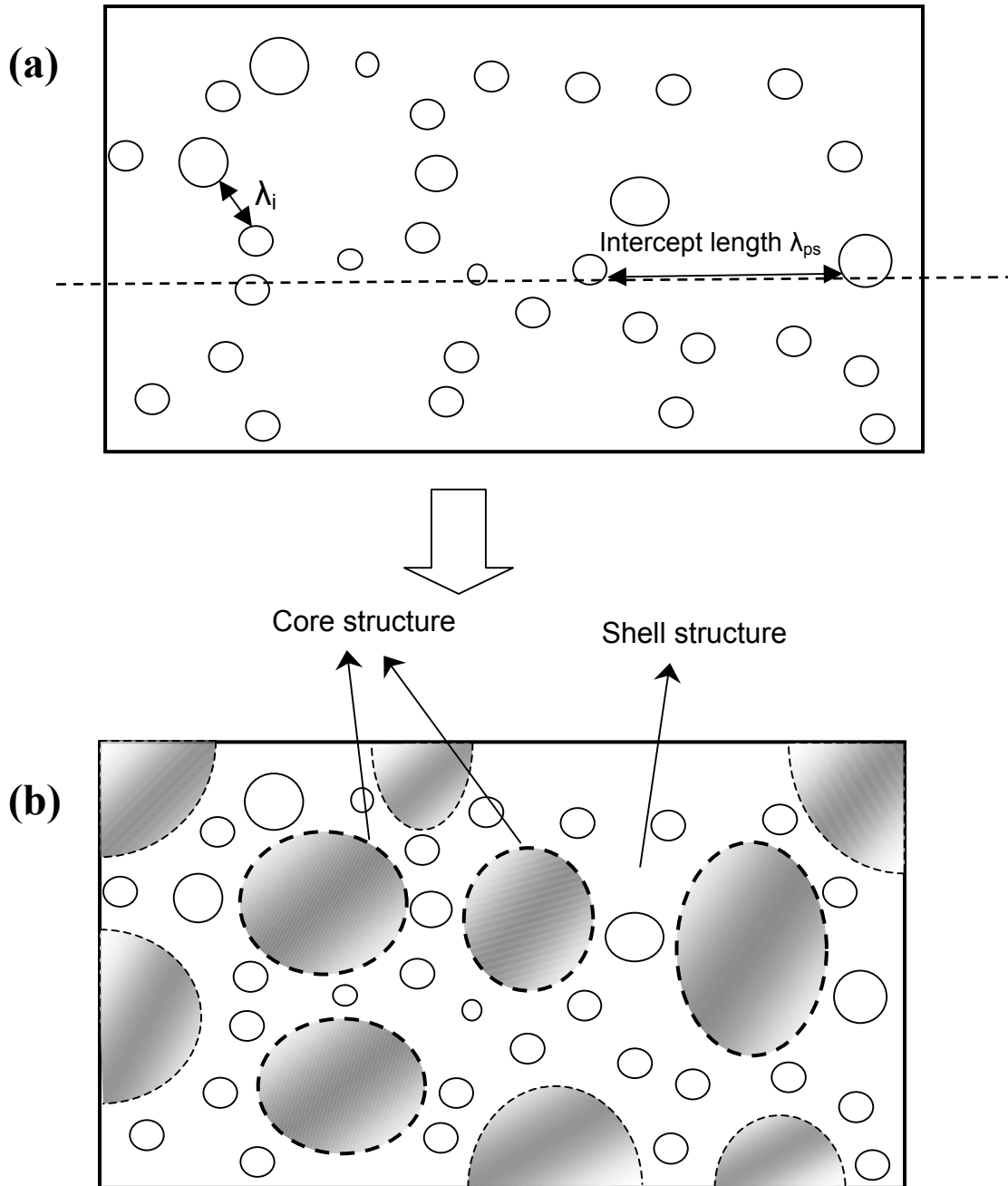


Figure 39: The illustration of non-random pore arrangement. (a): The comparison of intercept lengths λ_{ps} and the distances λ_i needed to calculate for λ_d . (b): The demonstration of cores and shells.

shrinks along with a decreased densification rate of the bulk material. In a structure with this pore arrangement, diffusion is more likely to happen between pores within the shells, instead of happening across the dense cores. However, the average inter-pore intercept length measured on

randomly applied lines will include distances across cores and thereby overestimate the diffusion length as the dense area growth leads to a lower exponential for the relationship between volume strain rate and the inverse of the pore separation. This would explain the decrease systematic decrease in slope for the pore separation during sintering.

To address the inability of simple pore separation intercept length to represent diffusion length, we proposed a new diffusion parameter which weights the distance between two neighboring pores in the shell structure contrary to the simple pore separation. The commonly measured intercept length λ_{ps} and the distance λ_i representing the “diffusion short-cuts” in an aggregated structure are represented in Fig. 39 (a). We proposed that after core-shell structures form during the initial stage of sintering of an aggregated powder only the shell structures will contribute to further densification of zirconia ceramics, while the dense cores do not strongly participate in this process. In other words, diffusion between pores in the shells separated by short distances dominates the densification while mass transport across the dense areas is less significant. That being said, it is crucial to integrate a parameter that can represent the average diffusion length for mass during sintering of a core-shell structure. Therefore, a new parameter which integrates all the local distances to coordinating pores should be developed.

Figure 40 is a schematic drawing aimed at explaining how this new parameter is defined. Assuming that there were 5 nearest neighboring pores around the center pore A. As seen, not all pores will be considered as the nearest neighboring pores, such as pore 6, pore 7 and pore 8. If this structure is subject to pore boundary tessellation only the pores in tessellation cells that share a boundary with the centering pore A will be considered as the nearest neighboring pores.

During sintering, mass would be transported into the center pore A from the areas between the pores. In order to fill the center pore, Flux J needs to be transported. If the mass

transported from the area between pore A and pore 1 is $J_1 = kc/\lambda_1$, then similar expression can be generated for all the other surrounding pores, $J_2 = kc/\lambda_2$, $J_3 = \dots$. Where k and c are constants, λ_i is the half distance between the edge of center pore A and the edge of the neighboring pore i. Then, the flux from areas between pore A and all nearest neighboring pores

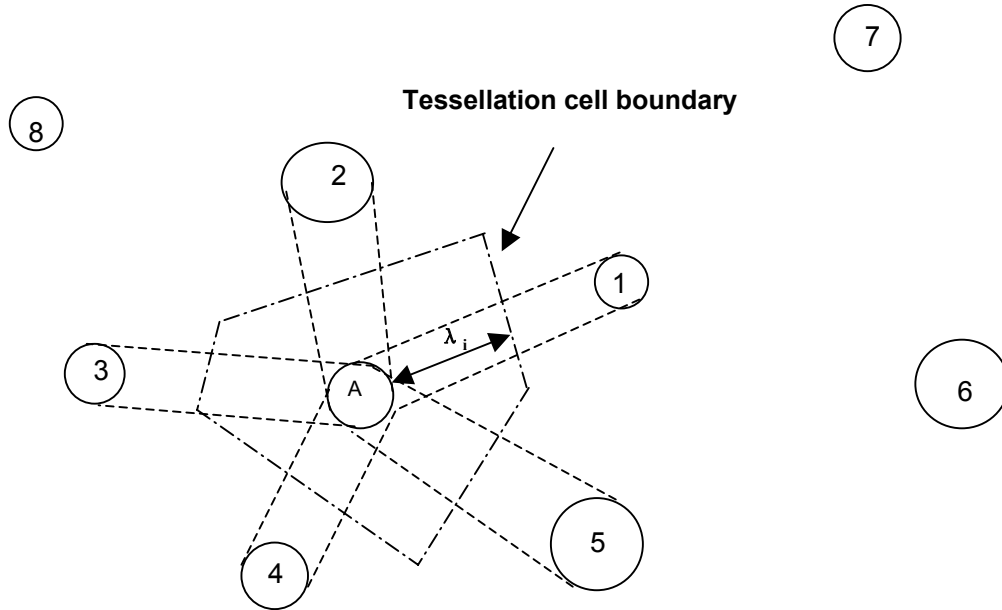


Figure 40: The schematic drawing of pore arrangement and how the effective diffusion distance can be defined.

is $J = J_1 + J_2 + \dots = kc(1/\lambda_1 + 1/\lambda_2 + \dots) = nkc(1/\lambda_d)$. Thus, this new proposed parameter defines the effective diffusion distance λ_d such that

$$\frac{n}{\lambda_d} = \sum_i \frac{1}{\lambda_i} \quad \text{Equation (6.3)}$$

where n is the number of neighboring pores.

As we can see from equation (6.3), neighboring pores which are closer to the center pore contribute more in mass transportation, since smaller λ_i values result in larger $1/\lambda_i$ values; on the other hand, those pores which are far away from the center pore can have little effect on the calculation of λ_d since $1/\lambda_i$ could be too small. This parameter was measured for isothermal sintering of TZ-3YB, HA and the alumina sintered in the previous study.

6.3 EFFECTIVE DIFFUSION DISTANCE OF SYSTEMS UNDER STUDY

The effective diffusion distance, as defined in Equ. (6.3) for TZ-3YB is 0.184, 0.232, 0.358 and 0.546 μm , respectively, for samples sintered at 1275°C for 0.5, 1, 5 and 10 hours. These values are relatively low compared with the values of pore separation, which were 0.631, 0.844, 2.023 and 3.851 μm , respectively. This difference is not surprising since we have demonstrated previously that the pore separation is an overestimation of the diffusion distance in

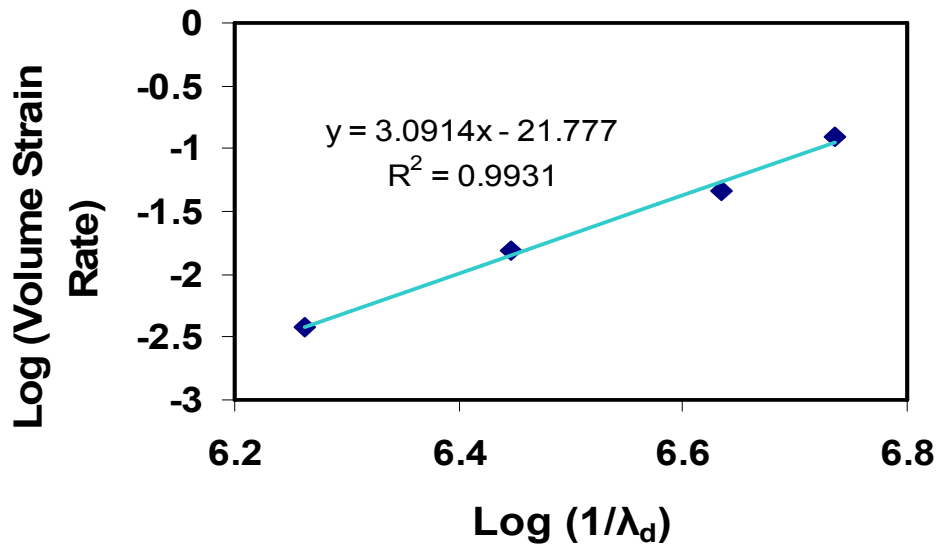


Figure 41: The plot of volume strain rate against inverse effective diffusion distance of TZ-3YB.

the core-shell structures observed in this study. The plot of volume strain rate against inverse effective diffusion distance of TZ-3YB ceramics is shown in Fig. 41. Compared with the change of slopes in the plot of volume strain rate against inverse pore separation shown in Fig. 30, the value of R^2 in Fig. 41 is very close to 1 (0.9931), which suggests the microstructure change of the aggregated structure during sintering is accounted for by this new parameter. Furthermore, the exponent value in Fig. 41 is 3.09, which is very close to 3, expected for volume diffusion controlled sintering in the “ideal” microstructures used in the sintering models.

The effective diffusion distance is also measured for HA. Fig. 42 shows the plot of volume strain rate against inverse effective diffusion distance. This plot also features a good R^2 value of 0.9938. The exponent value here is 3.45, somewhere between 3 and 4, which are the expected ideal value for either volume diffusion or grain boundary diffusion. Obviously, this value is inconsistent with the model and it is now necessary to discuss the origins of these exponents.

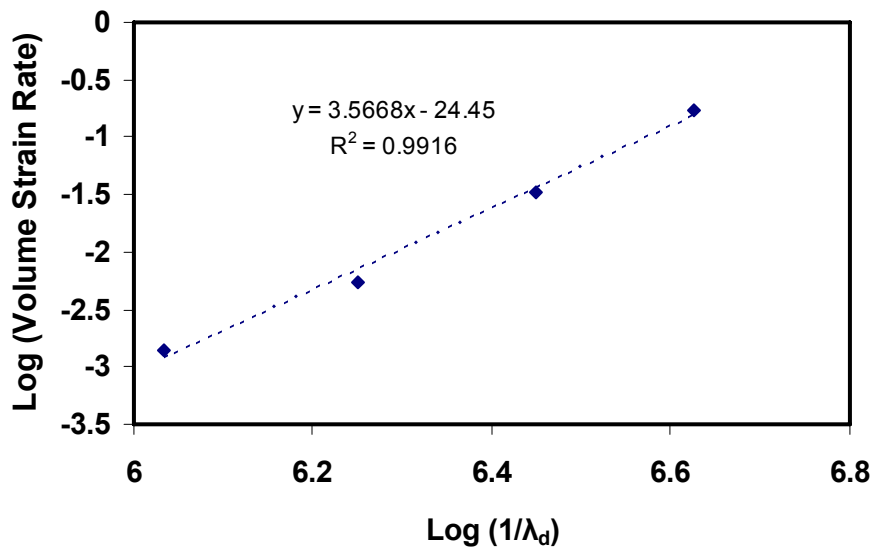


Figure 42: The plot of volume strain rate against inverse effective diffusion distance of HA.

According to the traditional models, the relationship between volume strain rate and inverse microstructure parameter is expected to be 3 by volume diffusion mechanism or 4 by grain boundary diffusion as indicated by Equ. (2.20)

$$-\frac{dL}{Ldt} = \frac{\gamma\Omega}{kT} \left(\frac{\Gamma_v D_v}{G^3} + \frac{\Gamma_b \delta D_b}{G^4} \right) \quad \text{Equation (2.20)}$$

Where G can be replaced by λ_d in aggregated structures. The first term in right side of Equ (2.20) describes volume diffusion and second term describes grain boundary diffusion. Based on energetics, at given temperature, normally, only one diffusion coefficient, D_v or D_b , dominates. The exponential dependence of the diffusion coefficients on temperature and the differences in activation energies result in a situation where comparable diffusion contributions would occur only in a very small temperature range. For most temperatures the contribution of only one sintering mechanism would dominate. The difference in exponent values between the two terms on the right side of equation originates from the difference in width of the assumed flux field, which limits diffusion, for these two diffusion mechanisms. The derivation of two terms on right hand of Equ. 2.20 are now considered in more details as following. Because,

$$\frac{dL}{Ldt} = -\frac{J\Omega_a}{C_h C_a G^3} \quad \text{Equation (6.4)}$$

$$J = \frac{1}{2} j_{asb} \delta L_b + j_{asv} A_v \quad \text{Equation (2.13)}$$

And,

$$j_a = -\frac{D}{\Omega_a K_B T} \nabla(\mu_a - \mu_v) \quad \text{Equation (2.4)}$$

Also,

$$\nabla \mu_{a|s} = - \frac{\alpha \gamma \Omega_a C_k}{C_\lambda G^2} \quad \text{Equation (2.11)}$$

After substituting equations (2.14), (2.4) and Equ. (2.11) into Equ. (6.4), there is a G^5 in denominator of the terms in right hand for both mechanisms. Since L_b and A_v are assumed to scale with G and G^2 respectively, a G is cancelled in the denominator of grain boundary diffusion term while a G^2 is cancelled for the volume diffusion term. When grain boundary diffusion dominates, the limiting factor is the thickness of grain boundary, since flux is limited to grain boundary. In the models the thickness of grain boundary is a constant for a certain material system. The exponent value for grain boundary is thus 4 since the second term dominates in right hand side of Equ. (2.20). When volume diffusion dominates, the flux flowing into a pore is limited only by the pore diameter, which can be related to grain diameter by the model geometry. Since that relationship between densification rate and grain size was derived from the traditional geometry model, it does not apply to aggregated structure directly. The most significant difference between the traditional geometry model structure and the aggregated structure under this study is that, in traditional models, it was assumed that there is only one grain separating any two nearest neighbor pores, while in the aggregated structure multiple grains exist between two nearest neighboring pore. Thus, in aggregated structures, the width of flux field is also changed from the traditional models' structure. These changes are listed in Table 3.

Table 3: flux field width of grain boundary diffusion and volume diffusion in different microstructures.

| <i>Width of flux field</i> | Grain Boundary Diffusion | Volume Diffusion |
|---|---|-------------------------|
| Traditional models: Single grain between pores | Thickness of <u>one</u> grain boundary | Pore diameters |
| In aggregated structure: Multiple grains between pores | Thickness of <u>multiple</u> grain boundaries | Pore diameters |

It is clear that there is no difference in the exponent value between these two structures if volume diffusion dominates, since the diffusion field is constrained by the pore diameter, which will not be effected by number of grains between pores. However, in the case of grain boundary diffusion, the exponent value will change for same material system when the number of grains between nearest neighboring pores changes. In the case when two pores are separated by only one grain, as shown in Fig. 43 (a), the thickness of this single grain boundary will limit the flux field when grain boundary diffusion dominates. In the other case, as shown in Fig. 43 (b), the limiting factor becomes the thickness of multiple grain boundaries, since multiple diffusion paths exist and contribute to the flux. Let us consider an extreme case. If there is a system with aggregated structure and extremely fine grains compared to pore size, one can imagine that a large number of grain boundaries will terminate at the pore and the flux field will be limited by the pore diameter again and the exponent value will be close to 3 even if grain boundary diffusion dominates. It is not difficult to conclude that the exponent value of a structure demonstrated in Fig. 43 (b) will be between 3 and 4 for grain boundary diffusion in an aggregated structure depending on the ratio of the pore size to the grain size.

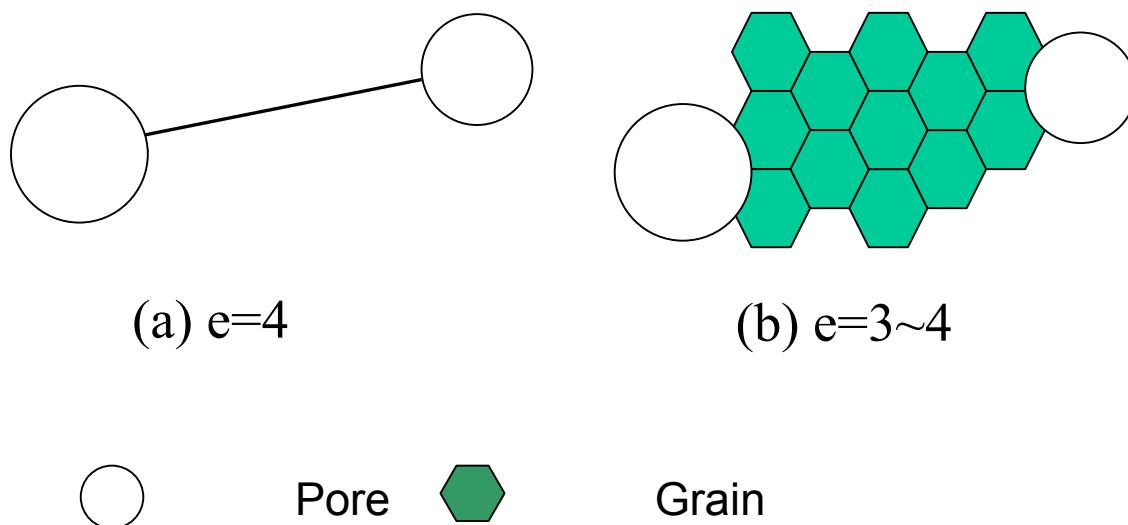


Figure 43: Simple one dimensional model: (a) pores separated by single grain. (b) pores are separated by multiple grains.

Now let us try to explain it from equations. Equation (2.13) can also be written as

$$J = j_{asb} A_b + j_{asv} A_v \quad \text{Equation (6.5)}$$

The traditional models are based on DeHoff cell construction that assumes pores exist in every grain edges, as demonstrated in Fig. 5, or in a two dimensional model as seen in Fig. 44,

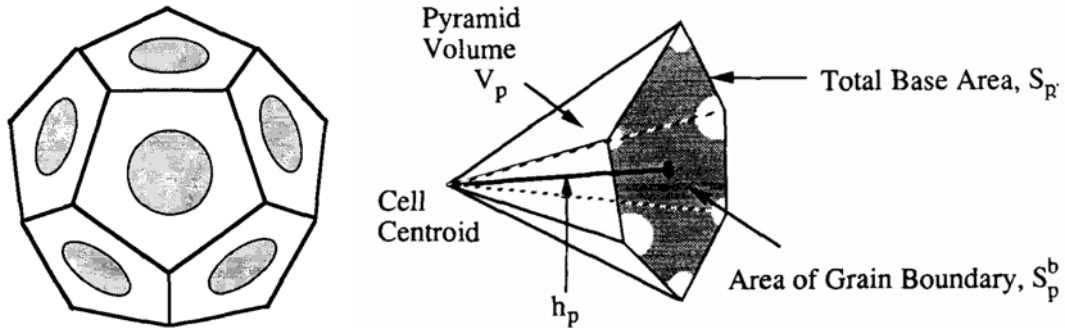


Figure 5: The: Cell construction in the left showing a grain and its associated porosity, at initial stage sintering (after DeHoff). The shaded areas represent solid contact areas between cells, i.e., grain boundaries. Pyramid subgeometry of a cell is shown in the right side.

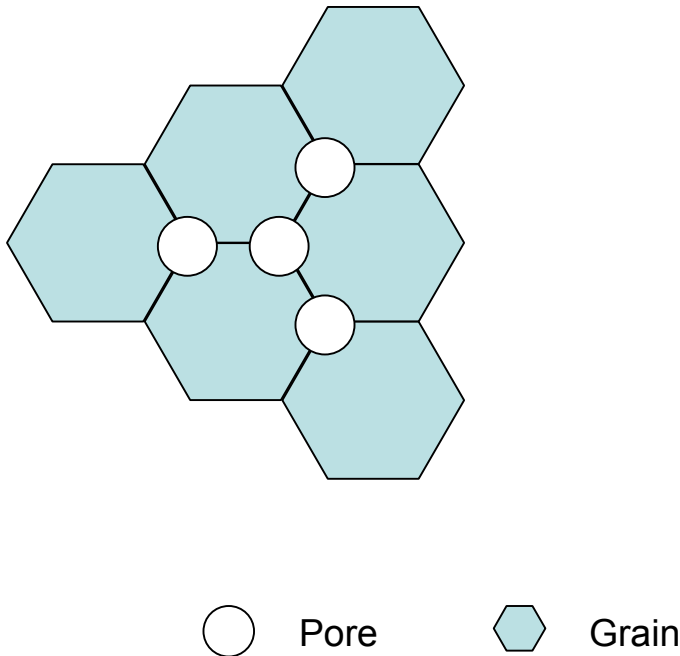


Figure 44: Simple two dimensional model from traditional models with pores located on every grain edges.

which has a coordination number of 3 for grains around a pore. In addition, another assumption is that pore channels do not shrink along their length and no pore elimination occurs during

sintering so the coordination number of grains around a pore never changes during intermediate and final stages of sintering. Or in other word, the pattern of grain-boundary pore interface is fixed. For any specific material, the thickness of grain boundary is a constant. This leaves L_b , which is proportional to G , the only variable in A_b . However, our measurement shows the ratio of average pore size over grain size of HA samples changes from 0.82 to 0.94 (Fig. 45), which

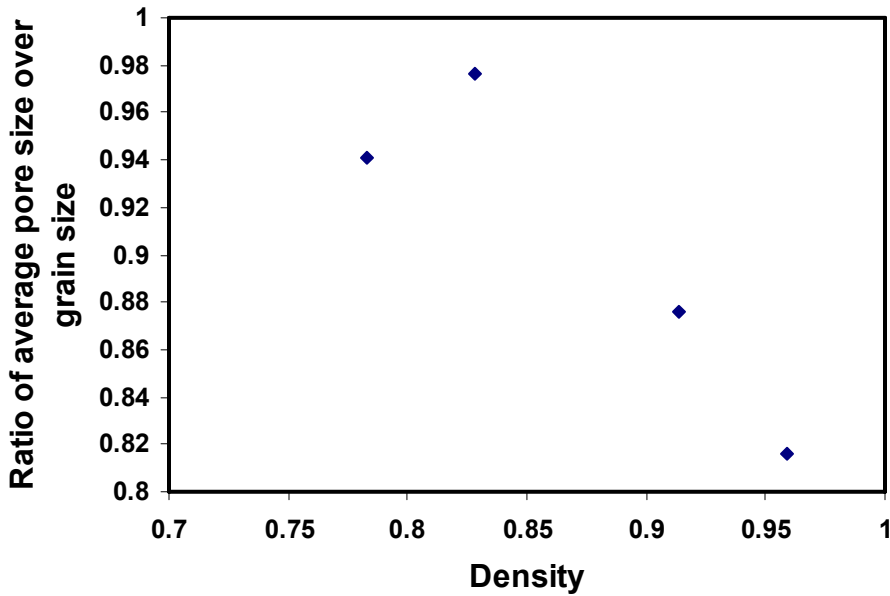


Figure 45: Ratio of average pore intercept length over grain intercept length of HA samples.

indicates the average coordination number of grains around a pore is above 3 and more importantly, the number of grains around a pore changes during sintering. This will add more complexity to the problem. As the ratio of pore size over grain size increases, the amount of grain boundary emptying into a pore will increase. When the extreme condition is reached, A_b equals A_v , and both are proportional to G^2 . So, for the aggregated structure with pore elimination or pore section elimination during sintering, A_b can be written as

$$A_b = C'_b \cdot G \cdot G^\beta \quad \text{Equation (6.6)}$$

where C'_b is a constant, G is the mean grain diameter and β is a variable, which approaches one when the ratio of A_b over A_v approaches to 1. When there is no pore section elimination, β would be 0. According to this equation, for grain boundary diffusion dominating systems, the exponent value of log volume strain rate against log inverse effective diffusion distance is 4 when no pore section elimination occurs. When pore section elimination exists during sintering, the exponent value approaches 3 as the ratio of pore size to grain size grain size becomes infinitely large.

Besides the two systems studied in this work, the effective diffusion distance was also measured for some previous studied alumina ceramics. The SEM images of sintered slip cast alumina left by a former student, Richard McAfee were analyzed using methods described in this work and the plot of volume strain rate against inverse effective diffusion distance is shown in Fig. 46. This was done for alumina slip cast with the same powder in the dispersed and the flocculated condition and sintered isothermally at 1350°C.

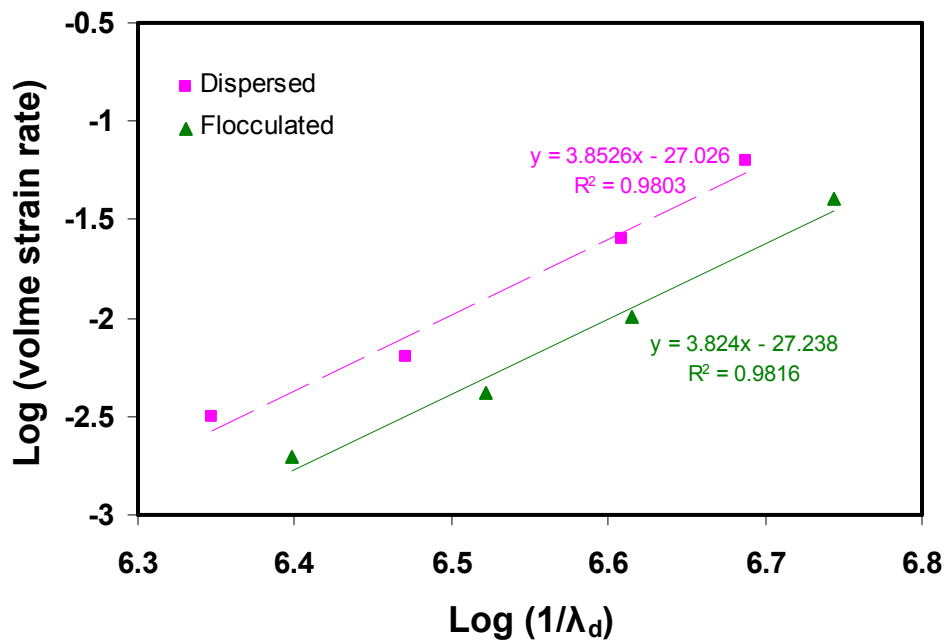


Figure 46: plots of volume strain rate against inverse effective diffusion distance of alumina ceramics.

Good R^2 values are observed in both these plots, which are 0.9803 and 0.9816 for dispersed and flocculated alumina and the exponent values were 3.85 and 3.82 for the dispersed and the flocculated alumina, respectively. The small difference of the exponent values (0.03) between these two systems indicates that even though the slip cast conditions are different, the densification behavior during sintering are very similar for this same powder. The exponent values here are also between 3 and 4, suggests these alumina powders densified by grain boundary diffusion. This result is consistent with previous study of Zhou and Harmer which argues that grain boundary diffusion dominated in sintering of alumina powder.⁵⁷ Since the exponent values are closer to 4 than that of HA system, then the ratio of average pore size over grain size should be lower based on argument proposed here. Indeed, this trend for ratio of pore size over grain size is clearly demonstrated by Fig. 47.

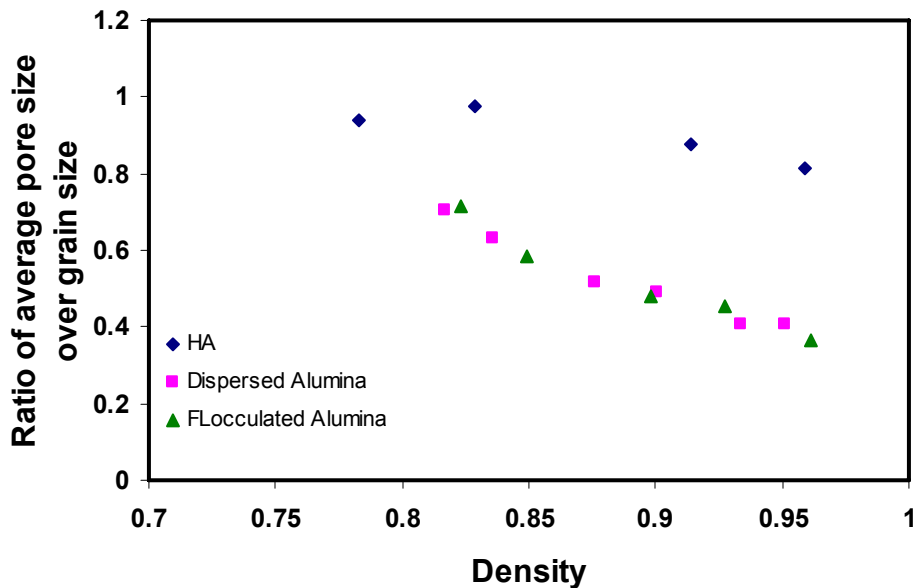


Figure 47: Comparison of Ratios of average pore separation intercept length over grain intercept length as isothermal sintering time increase between HA and alumina samples.

Based on above statement, the exponent value of TZ-3YB of 3.09 suggests this material sintered at 1275 °C densifies by volume diffusion. This result agrees with the conclusions of

Okamoto et al. who performed creep experiments on tetragonal zirconia containing 3mol% Y_2O_3 . Their results suggested creep was controlled by volume diffusion which would also be expected to control sintering. The exponent value of HA is 3.45, which indicates HA sintered at 1100 °C densifies by grain boundary diffusion. The exponent values of the two α -alumina ceramics processed under different processing conditions are around 3.8, which suggests that alumina powder densifies by grain boundary diffusion.

7.0 CONCLUSIONS

The following conclusions can be summarized from this work:

1. Sintering of aggregated nanocrystalline ceramic powders at low temperature results in non-ideal microstructures. SEM images of polished surfaces show that in these ceramics nearest neighboring pores are separated by multiple grains. Intercept length measurement quantitatively confirm that the pore separations are larger than grain sizes,
2. For ceramics with multiple grains between pores we found that the inter-pore distance can scale the diffusion distance better than grain size. To be specific, plots of volume strain rate against inverse microstructural parameters show the exponent values of grain size are too high. In contrast, the exponent value of pore separation is closer to the expected value of 3 or 4 derived from traditional models.
3. In sintered aggregated structure, dense regions grow as isothermal sintering time increases. The power law relationship between volume strain rate and diffusion distance does not fit the data well for pore separation due to change of microstructure during sintering. Since diffusion between pores in more porous regions dominates densification, average inter-pore intercept length based on the stereological definition of pore separation would be an overestimation for diffusion distance in an aggregated structure.

4. A new effective diffusion distance was defined in this work based on pore boundary tessellation. Good fitting relationships between densification rate and the effective diffusion distance λ_d was found, suggesting λ_d may allow a simple one dimensional flux model to be used to analyze densification of inhomogeneous structures created from aggregated powders.
5. The exponent value for plots of volume strain rate against inverse effective diffusion distance is related to diffusion mechanisms. The exponent value is expected to be 3 for volume diffusion. For grain boundary diffusion, it is expected to be somewhere between 3 and 4. As the ratio of average pore size over grain size decreases, the value approaches to 4.
6. The exponent value for plots of volume strain rate against inverse effective diffusion distance of TZ-3YB suggests this powder densifies by volume diffusion. The values of HA and α -alumina suggest they densify by grain boundary diffusion.

8.0 SUGGESTED FUTURE WORKS

1. Corrections to the effective diffusion distance should be explored for the case of grain boundary diffusion.
2. The correlations should be explored between the grain size to pore size ratio and effective diffusion distance exponent for a system known to sinter by grain boundary diffusion.
3. 3D microstructural analysis by serial sectioning (Focus Ion Beam) should be performed to relate the tessellation of two dimensional section data to three dimensional characteristics of the microstructure. This would be used to study how elimination of pore sections is related to changes in the topology of the pore structure.
4. *In-situ* experiments should be performed to determine the nature of the rearrangement of particles or grains during the intermediate stage of sintering to determine the rearrangement mechanisms that lead to pore section elimination and formation of core-shell structures.

BIBLIOGRAPHY

- ¹ Exner, H. E., "Principles of Single Phase Sintering," *Reviews in Powder Metallurgy and Physical Ceramics*, 1, 1-4, 1979, pp. 1-251.
- ² Burke, J. E. and J. H. Rosolowski, "Sintering," General Electric Technical Information Series, General Electric Company, Schenectady, NY, 1973.
- ³ Olevsky, E. A., "Theory of Sintering; From Discrete to Continuum," *Materials Science and Engineering*, Vol. R23, No.2, 1998, pp. 41-100.
- ⁴ Pask, J. A., and A. G. Evans ed., *University Conference on Ceramics; Ceramic Microstructures '86: Role of Interface*, "Powders, Interfaces, and Processing: Alumina as a Case Study by A. Roosen, S. Sumita and H. K. Bowen," Plenum, NY, 1987, pp. 433-446.
- ⁵ Reed, J. S., *Introduction to the Principles of Ceramic Processing* New York: Wiley-Interscience, 1988, p. 87.
- ⁶ E. A. Olevsky "Theory of sintering, from discrete to continuum" *Mat. Sci. & Eng.*, **R23**, 41-100 (1988).
- ⁷ J. Besson and M. Abouaf (1992). "Rheology of porous alumina and simulation of hot isostatic pressing" *J. Am. Ceram. Soc.*, **75** [8], 2165-2172.
- ⁸ R. K. Bordia and G. W. Scherer (1988). "On constrained sintering-I. constitutive model for a sintering body" *Acta Metall.*, **36** [9], 2393-2397.
- ⁹ W. D. Kingery and M. Berg (1955). "Study of the initial sintering of solids by viscous flow, evaporation-condensation and self diffusion" *J. Appl. Phys.*, **26**, 1205.
- ¹⁰ R. L. Coble (1961). "Sintering crystalline solids. I. intermediate and final state diffusion models" *J. Appl. Phys.*, **32** [5], 787-792.
- ¹¹ H. Reidel and B. Blug (2001). A comprehensive model for the solid state sintering ad its application to silicon carbide. pp. 49-70, in *Multiscale Deformation and Fracture in Materials and Structures*, the James R. Rice 60th Anniversary Volume. Edited by T. J. Chuang and J. W. Rudnicki. Kluwer Academic Publishers, Boston.

-
- ¹² O. Gillia and D. Bouvard (2000). “Phenomenological analysis of densification kinetics during sintering: application to WC-Co mixtures” *Materials Science and Engineering*, **A279**, 185-191.
- ¹³ P. Z. Cai, G. L. Green, (1997). “Determination of the mechanical response of sintering compacts by cyclic loading dilatometry” *J. Am. Ceram. Soc.*, **80** [2], 445-452.
- ¹⁴ V. Tikare, M. Braginsky, J. Arguello and T. Garino, (2003). “Numerical simulation of sintering at multiple length scales” Presented at 3rd *International conference on Science, Technology and Applications of Sintering*, September 15-17, State College, PA.
- ¹⁵ Y. Chiang, D. Birnie III, W. D. Kingery, “Physical Ceramics: Principles for Ceramic Science and Engineering”, John Wiley & Sons, Inc.
- ¹⁶ Okamoto, J. Ieuji, Y. Yamada, K. Hayashi and T. Nishikawa, “Creep Deformation of Ytria-Stabilized Tetragonal Zirconia (Y-TZP)”; *The Amer. Ceram. Soc.*, Columbus (OH) 1988, p. 565
- ¹⁷ R. S. Gordon, “Ambipolar Diffusion and its application to Diffusion Creep”; pp. 445-64 in *Mass Transport Phenomena in Ceramics* (Materials Science Research, vol 9). Edited by A. R. Cooper and A. H. Heuer. Plenum, New York, 1975
- ¹⁸ Y. Sakka, Y. Oishi, and K. Ando, “Zr-Hf Interdiffusion in Polycrystalline Y₂O₃-(Zr+Hf)O₂”; *J. Mater. Sci.*, **17** [11] 3101-3105 (1982)
- ¹⁹ R. J. McAfee, Jr., “A Study of Microstructural Evolution During Sintering Using Tessllation”, Ph. D. Thesis, Univ. of Pittsburgh (2004).
- ²⁰ H. F. Fischmeister, and E. Arzt, “Densification of powders by particle deformation” *Powder Metallurgy*, **26** 82-88 (1983).
- ²¹ M.F. Ashby, “A First Report on Sintering Diagrams,” *Acta Metall.*, **22** 275-89 (1974).
- ²² I. Nettlehip, B. R. Patterson and W. S. Slaughter, “Evolution of Average Microstructural Properties in the Final Stage Sintering of Alumina”, *J. Am. Ceram. Soc.*, **86** [2] 252-56 (2003).
- ²³ W. S. Slaughter, I. Nettlehip, M. D. Lehigh, and P. P. Tong, “A Quantitative Analysis of the Effects of Geometric Assumption in Sintering Models”, *Acta Mater.*, **45** [12] 5077-86 (1997).
- ²⁴ Weiser, M. W., and L. C. De Jonghe, “Rearrangement During Sintering in Two-Dimensional Arrays,” *J. Am. Soc.*, Vol. 69, No. 11, 1986, pp. 822-826.
- ²⁵ R. W. Rice, W. R. Grace and Co. Conn., “Evaluation and Extension of Physical Property-Porosity Models Based on Minimum Solid Area” *J. of Mat. Sci.*, **31** (1996) 102-118.

-
- ²⁶ J. D. Hansen, R.P. Rusin, M.H. Teng and D.L. Johnson, “Combined Stage Sintering Model,” *J. Am. Ceram. Soc.*, **75** 1129-35 (1992).
- ²⁷ J. Zheng and J. S Reed, “The Different Roles of Forming and Sintering on Densification of Powder Compacts,” *Am. Ceram. Soc. Bull.*, **71** [9] 1410–16 (1992).
- ²⁸ C. Herring, “Surface Tension as a Motivation for Sintering”, ch. 8, pp. 143-79 in *The Physics of Powder Metallurgy*. Edited by W. E. Kingston. McGraw-Hill, New York, 1951.
- ²⁹ R.T. DeHoff, “A Cell Model for Microstructural Evolution during Sintering”, pp. 23-34 in *Sintering and Heterogeneous Catalysis*. Edited by G.C. Kuczynski, A. E. Miller, and G. A. Sargent. Plenum Press, New York, 1984.
- ³⁰ Ph. Buffat, J-P. Borel, *Phys. Rev. A* **13**, 2287 (1976)
- ³¹ C. J. Coombes, Thesis, University of London, 1969. C. J. Coombes, *J. Phys.* **F 2**, 441 (1972).
- ³² M.N. Rahaman, L.C. DeJonghe and M.Y. Chu, “Effect of Green Density on Densification and Creep During Sintering,” *J. Am. Ceram. Soc.*, **74** 514-19 (1991).
- ³³ C. P. Cameron, R. Raj, “Better Sintering through Green-State Deformation Processing”, *J. Am. Ceram. Soc.*, **73** 2032-37 (1990).
- ³⁴ K. G. Ewsuk, D. T. Ellerby, G. B. DiAntonio, “Analysis of Nanocrystalline and Microcrystalline ZnO Sintering Using Master Sintering Curves”, *J. Am. Ceram. Soc.*, **89** 2003-2009 (2006).
- ³⁵ Pai-Liu Chen and I-Wei Chen, “Sintering of Fine Oxide Powders: I, Microstructural Evolution” *J am. C. Soc.* **79** [12] 3129-41, 1996
- ³⁶ J. Zheng, J. S. Reed, “Effects of Particle Packing Characteristics on Solid-State Sintering” *J. Am. Ceram. Soc.*, **72** 810-817 (1989).
- ³⁷ Yeh and M.D. Sacks, “Effect of Green Microstructure on Sintering of Alumina,” pp.309-31 in *Ceramic Transactions, vol 7, Sintering of Advanced Ceramics*. Edited by C.A. Handwerker, J.E. Blendell and W.A. Kaysser, American Ceramics Society, Westerville, OH, 1990.
- ³⁸ F. F. Lange, “Sinterability of Agglomerated Powders,” *J. Am. Ceram. Soc.* **67** 83 -89 (1984).
- ³⁹ J. Li and Y. Ye, “Densification and Grain Growth of Al₂O₃ Nanoceramics During Pressureless Sintering”, *J. Am. Cream. Soc.*, **89** [1] 139-143 (2006).
- ⁴⁰ I.-W. Chen and X.-H. Wang, “Sintering Dense Nanocrystalline Ceramics Without Final-Stage Grain Growth,” *Nature*, **404** [6774] 168–71 (2000).

-
- ⁴¹ X. Wang, P. Chen, and I. Chen, "Two-Step Sintering of Ceramics with Constant Grain-Size, I. Y_2O_3 " *J. Am. Ceram. Soc.*, **89** [2] 431-437 (2006).
- ⁴² I. Nettleship, T. Chen, and K. Ewsuk, "Microstructure evolution in ZrO_2 -3mol% Y_2O_3 during Isothermal Sintering", *Journal of American Ceramic Society*, **90**, 3793 (2007).
- ⁴³ R. Stevens, "Zirconia and zirconia ceramics", Magnesium Elektron Ltd, second edition.
- ⁴⁴ P.N. Kumta, "Ceramic Biomaterials", *An Introduction to Biomaterials*, CRC Press, pgs. 311-340, 2006.
- ⁴⁵ J. M. Buchanan, "Nineteen Year review of hydroxyapatite ceramic coated hip implants: A clinical and histological evaluation," *Key engineering materials* vol 361-363 pages 1315 to 1318 (2008).
- ⁴⁶ <http://accuratus.com/alumox.html>
- ⁴⁷ Weibel, E. R., *Stereological Methods Volume 1, Practical Methods in Biological Morphometry* New York: Academic Press, 1979.
- ⁴⁸ Vander Voort, G., ed., Applied Metallography, "Problem Solving Using Quantitative Stereology, by R. T. DeHoff" New York: Van Nustrand-Reinhold Company, 1986, pp. 89-99.
- ⁴⁹ Exner, H. E. and H. P. Hougardy, *Quantitative Image Analysis of Microstructures: A Practical Guide to Techniques, Instrumentation, and Assessment of Materials*, Stuttgart: Verlag, 1988, p. 10.
- ⁵⁰ Dehoff, R. T. and F. N. Rhines, "Quantitative Microscopy," McGraw-Hill, NY, 1968.
- ⁵¹ Cahn, R. W. and P. Haasen ed., Physical Metallurgy: 4th Revised and Enhanced Edition, "Qualitative and Quantitative Surface Microscopy by H. E. Exner," Elsevier, 1996 pp. 996-1032.
- ⁵² Y Okamoto, J. Ieuji, Y. Yamada, K. Hayashi and T. Nishikawa, "Creep Deformation of Ytria Stabilized Tetragonal Zirconia," *Advances in Ceramics*, Vol 24, Science and Technology of Zirconia III, pp. 565-571 edited by S. Somiya, N. Yamamoto and H. Hanagida, published by American Ceramics Society, (1988).
- ⁵³ H. Su and D.L. Johnson, "Master Sintering Curve: A practical Approach to Sintering," *J. Am. Ceram. Soc.*, **79** 3211-17 (1996).
- ⁵⁴ C.D. Sagel-Ransijn, A.J.A Winnubst, A.J. Burgraaf, H. Verweij, "Grain Growth in Ultra-fine Grained Y-TZP Ceramics," *J. Euro. Ceram. Soc.*, **17** 1133-1141 (1997).

-
- ⁵⁵ I. Nettleship, R. McAfee “Microstructural Pathway for the Densification of Slip Cast Alumina” *Mater. Sci. Eng. A*, **352** 287-293 (2003).
- ⁵⁶ K.A. Berry and M.P. Harmer, “Effect of MgO Solute on Microstructure Development in Al₂O₃,” *J. Am. Ceram. Soc.*, **69** 143-149 (1986).
- ⁵⁷ J. Zhao and M.P. Harmer, “Effect of Pore Distribution on Microstructure Development: III, Model Experiments,” *J. Am. Ceram. Soc.*, **75** 830-43 (1992).